Die approbierte Originalversion dieser Diplom-/Masterarbeit ist in der Hauptbibliothek der Technischen Universität Wien aufgestellt und zugänglich.
http://www.ub.tuwien.ac.at

The approved original version of this diploma or master thesis is available at the main library of the Vienna University of Technology.
http://www.ub.tuwien.ac.at/eng

_____
Unterschrift des Betreuers

TECHNISCHE UNIVERSITÄT WIEN

DIPLOMARBEIT

Combined Polarisation and Absorption Imaging for experiments with Nanofiber trapped atoms

Ausgeführt am Atominstitut
der Technischen Universität Wien

unter der Anleitung von
Univ.Prof. Dr. Arno Rauschenbeutel

durch

Martin Blaha, BSc

Matrikelnummer 1025913
Anningerstraße 76-78/4, 2353 Guntramsdorf

Wien, am 11. Mai 2016

_____
Unterschrift Student

Declaration

I hereby declare that except where specific reference is made to the work of others, the contents of this thesis are original and have not been submitted in whole or in part for consideration for any other degree or qualification in this, or any other university. This thesis is my own work and contains nothing which is the outcome of work done in collaboration with others, except as specified in the text and Acknowledgements.

Martin Blaha
May 2016

Acknowledgements

First I would like to acknowledge Prof. Dr. Arno Rauschenbeutel for the great opportunity of being part of his group, contributing in setting up a new exciting experiment and learning about a fascinating topic in physics.

I would further thank my colleagues Jakob Hinney, Adarsh Parsad, Samuel Rind and Dr. Christoph Clausen for the interesting and instructive discussions we had and the always warm, pleasant and conducive working environment. I would further acknowledge the whole group of Applied Quantumphysics for their friendly admission into the group and their kind support. Additionally I would thank in particular Dr. Christoph Clausen for the help of correcting this thesis, helping to organize my thoughts on this topic and his patient and helpful support with any question I had.

I would like to thank my best friends, Dominik Eberle and Florentina Heinrich for their support and effort to keep my live in balance. I further thank my student colleagues for the past years of mutual challenges and achievements and the strong friendship that was built this way.

Finally I will acknowledge my family for the loving support during my education, making it possible to fully concentrate on my physics studies.

Abstract

In the group of Prof. Dr. Arno Rauschenbeutel, a new atom-light interface is implemented to work as an optical fiber-component for quantum information processing and communication. The key ingredient of this interface is an optical nanofiber, a fiber with a sub-wavelength diameter, that is used to trap and interface cold atoms with guided light in the fiber. The goal of this experiment is to trap Cesium atoms along the fiber to yield suitable optical densities for many quantum protocols such as quantum memories (OD $\approx$ 100 to 300). One crucial requirement for stable trapping is precise control over the local polarization of the nanofiber-guided light fields, as well as the characterization of the atomic cloud used to load the nanofiber trap. For this, fluorescence imaging of the nanofiber and absorption imaging of the magneto-optically trapped atom-cloud was implemented to characterize and optimize the cooling and loading of atoms into the dipole trap. The imaging system allows for determining the position and shape of the cloud, measuring the temperature of the atoms, and adjusting the polarization of the trapping light.

Abstract

In der Gruppe von Prof. Dr. Arno Rauschenbeutel ist die Verwirklichung einer neuen Atom-Licht-Schnittstelle als faser-optische Komponente für die Quanteninformationsverarbeitung und Quantenkommunikation geplant. Der Hauptbestandteil des Experiments ist eine optische Nanofaser - eine Faser mit einem Durchmesser kleiner als die Wellenlänge des darin geführten Lichts - welche dazu benutzt wird kalte Atome zu fangen und an das geführte Licht zu koppeln. Das Ziel dieses Experiments ist es Cäsiumatome entlang der Faser zu fangen, um für Licht in der Faser eine hohe optische Dichte von 100 bis 300 zu erreichen. Dies ist für eine erfolgreiche Implementierung vieler quantentechnologischer Protokolle wie zum Beispiel Quantenspeicher erforderlich. Eine Voraussetzung für eine stabile Nanofaser-basierte Falle ist eine genaue Kontrolle über die lokale Polarisation des in der Faser geführten Lichtes, sowie die Charakterisierung der Atomwolke die zum Laden der Nanofaser-Falle verwendet wird. Zu diesem Zweck wurde eine Abbildungstechnik implementiert, welche eine Untersuchung der Faser mittels Fluoreszenzabbildung und eine Untersuchung der Atomwolke in einer magneto-optischen Falle mittels Absorptionsabbildung erlaubt. Auf diese Weise kann der Kühlvorgang und das Laden der Nanofaser-Falle überwacht und optimiert werden. Das kombinierte Abbildungssystem erlaubt die Feststellung von Größe, Form, sowie Temperatur der Atomwolke als auch die Polarisation des Fallenlichts auszurichten.

Table of contents

Summary and Outlook **xii**

Introduction **xiii**

1 Nanofiber based Traps **1**
1.1 The nanofiber 1
1.2 Optical Nanofiber Traps 3
1.2.1 Electromagnetic fields and mode structure 3
1.2.2 Dipole interaction and dipole trapping 6
1.2.3 Geometry of the Nanofiber trap 8

2 Cooling setup **13**
2.1 Preparation of Cesium atoms for loading into dipole traps 13
2.1.1 Trapping and cooling the atoms 13
2.2 Experimental implementation 18

3 Absorption Imaging **25**
3.1 Sensing atom-numbers and temperature of atom clouds 25
3.1.1 Absorption of light in optically dense atom vapour 25
3.1.2 Time of flight measurement 28
3.2 Design of the Imaging setup 29
3.2.1 Optical scheme 30
3.2.2 Horizontal setup 32
3.2.3 Vertical setup 38
3.2.4 Summary of experimental parameters 42
3.3 Summary and Outlook 42

4 Polarization Imaging **47**
4.1 Polarization in the nanofiber 47

4.2 Design of the imaging setup 51
4.3 Data Acquisition and Analysis 53
4.4 Summary and Outlook 55

References **63**

List of figures **65**

Appendix A Manual for Graphical User Interface **67**
A.1 Main Window and types of programmes 67
A.2 Polarization Analysis 68
A.2.1 1 Camera Capture 68
A.2.2 2 Camera Capture 70
A.3 MOT Analysis 71
A.3.1 MOT Live Analysis Programme 71
A.3.2 MOT Time of Flight Data Acquisition Programme 71

Appendix B Documentation on the code **75**
B.1 Data Acquisition and Analysis module 75
B.2 Graphical User Interface 76
B.3 Back-end Modules 77

Introduction

In the last few decades a new and prosperous field of physics emerged, devoted to the research and development of quantum technologies. Experimental techniques drastically improved, allowing for precise control over the quantum state of light and matter, and thus, atoms and photons are used as so called quantum bits (qubits) for encoding and processing information, harnessing quantum features like superposition and entanglement. The aim of quantum computation is to surpass the computational power of traditional computers. Even though establishing a universal quantum computer might still take some time, several devices that allow for simple computational operations and communication of quantised information have already been implemented and studied in great detail.

A possible platform for the implementation of such devices is currently investigated in the group of Prof. Dr. Arno Rauschenbeutel, where Cesium atoms are trapped and interfaced via optical nanofibers. An optical nanofiber is a tapered glass-fiber with a sub-wavelength diameter. This allows guidance of the light via the vacuum glass-boundary, where a significant part of the power propagates outside the fiber as evanescent field (Le Kien et al. (2004b)). Using a combination of differently detuned fields with respect to the D2 line of Cesium, one can create dipole traps in close vicinity of the fiber surface (Vetsch et al. (2012, 2010)). Thereby one gets very strong confined light guided in the fiber, which can be maintained over several millimetres, where the strong intensity of the evanescent field leads to a very strong interaction with the trapped atoms (Reitz et al. (2013)). Since atoms are perfectly suitable for qubit manipulation and photons qualify as excellent carriers of quantum information, optical-nanofibers are natural candidates for quantum light-matter interfaces.

A new experiment is currently being build alongside the composition of this thesis and will concentrate on trapping Cesium atoms using so called “magic” wavelengths as proposed by Le Kien et al. (2004a) and first demonstrated by Goban et al. (2012). Trapping atoms with magic wavelengths leads to state-insensitive trapping for certain transitions. It is proposed to achieve longer coherence times and higher numbers of

trapped atoms with these wavelengths, to create very high optical densities for the guided light. This can be used together with electromagnetically induced transparency (EIT) (Marangos (1998)) to establish a quantum memory (Sayrin et al. (2015)), where fiber-guided light is effectively stopped and retrieved at a later time, while maintaining its internal quantum state. Such a device would be very interesting for the implementation of quantum networks.

For trapping atoms with nanofibers, it is very important to have control over the trapping fields in the nanofiber, in particular over the polarization. Additionally, to load atoms into the shallow nanofiber dipole trap, cooling the atoms via a magneto-optical trap (MOT) and optical molasses is necessary. The work presented in this thesis concentrates on designing an imaging setup that allows for absorption imaging of the MOT and polarization measurements of the light guided in the nanofiber. This way determination of the MOT shape, position and temperature of the atoms as well as adjustment of the polarization of the trapping fields is possible.

This thesis is outlined as follows. In the first chapter I will elaborate on the physics behind the nanofiber based dipole trap and present the trapping configuration planned to use for this experiment. In the second chapter I will discuss the working principle of laser cooling and trapping of atoms. Furthermore, the experimental implementation of the magneto optical trap setup as used in the experiment, is described. Chapter three concentrates on absorption imaging, where I discuss how resonant light is absorbed by an atomic vapour and derive how to determine the temperature of an atom-cloud from acquired images. Based on that, I will discuss the physical and optical constraints that led to the design of the imaging setup and outline the experimental implementation. In the fourth chapter, I will introduce polarization measurements of scattered light from the nanofiber, taken via the same imaging setup, as a convenient way of determining the a-priori unknown polarization state of the fiber guided light and present the procedure of the polarization alignment. Finally preliminary results will be presented and discussed.

Chapter 1

Nanofiber based Traps

The nanofiber based trap, which confines Cesium atoms in a one dimensional lattice in close vicinity of the fiber, will be the backbone of this experiment. The trap consists of a two-coloured evanescent field surrounding the fiber, which forms an array of dipole traps on two sides of the fiber. For a good understanding of the trapping mechanism, and to motivate the reason for the need of absorption and fluorescence imaging, I will lay out the theoretical background for light guided in the fiber, the exact form of the dipole traps, and describe the experimental details of the experiment.

1.1 The nanofiber

In commercially available optical glass fibers, light is typically guided via total internal reflection at the glass-glass boundary of two layers of glass with two different refractive indices, named core and cladding. Similarly, a nanofiber guides the light along the glass-vacuum boundary. However a significant portion of the light is guided outside the fiber as an evanescent field, because the diameter of the fiber is smaller than the wavelength of the guided light. To preserve the mode structure of the guided light and guarantee an almost lossless transition, an adiabatic taper as sketched in Fig. 1.1 is necessary. In Fig. 1.2 one can see the transition from the normal sized part of the fiber into the so called waist, i.e. sub-wavelength part of the fiber. In the case of a nanofiber, the core is sufficiently thin to be neglected, while the cladding of the fiber acts as the new core and the vacuum surrounding the fiber takes the place of the cladding ($n = 1$).

Tapered optical fibers are produced via a flame brushing technique (Warken et al. (2007)), where a low pressure, hydrogen-oxygen flame capable of melting glass is brushed carefully over the glass fiber. At the same time, the fiber ends are carefully pulled

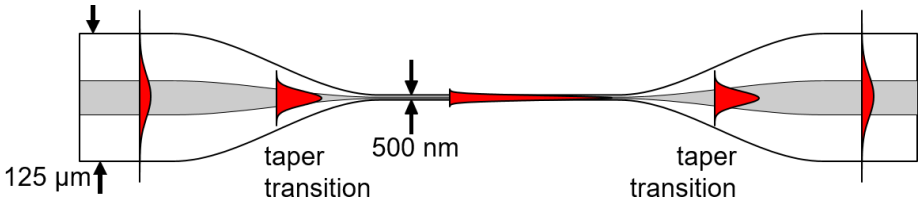


Fig. 1.1 The diameter of the nanofiber decreases adiabatically and confines the light guided in the fiber until a significant part of the light is guided as evanescent field. The strong confinement of the intensity in the nanofiber part (waist) leads to interesting quantum phenomena when the light interacts with atoms nearby.

apart in small steps and the fiber diameter in the heated region decreases. This can be done in a specially designed fiber pulling rig, where very high transmissions of about 99% through the nanofiber can be achieved in a reproducible way. Any perturbation on the fiber surface causes scattering and absorption of light, which leads to loss of guided light and therefore distortions of the trapping potential. Prominent scatterers that prevent building an excellent nanofiber based trap are dust particles settling on the fiber. When the fiber is placed in vacuum, thermal interaction with the environment is strongly suppressed and thus heating due to absorbed light by dust particles can lead to the destruction of the nanofiber. Therefore the whole process of pulling the fiber, mounting it on a suitable holder, and placing it inside the experimental setup has to be done in a dust free environment such as a laminar flow box.



Fig. 1.2 (top) Scanning electron microscope (SEM) picture of the taper transition from a standard fiber diameter to the nanofiber part. For a waist of 10 mm length the taper region is about 35 mm on each side to guarantee an adiabatic transition of the electromagnetic field mode. (bottom) Waist of the nanofiber, true to scale. Taken from (Rauschenbeutel (2009))

The experiment presented in this thesis is designed to contain a nanofiber with an extraordinary long waist of 10 mm and a radius of about 200 nm, which will be placed into ultra-high vacuum of about 10^9 mbar.

1.2 Optical Nanofiber Traps

For a better understanding of the particularities and difficulties of nanofiber based dipole traps, and to motivate the need of a precise knowledge of the polarization of guided light at the waist region of the fiber, I will outline the derivation for guided modes in nanofibers and present the most important results. A complete derivation can be found in Le Kien et al. (2004a,b) and Le Kien and Rauschenbeutel (2014)

1.2.1 Electromagnetic fields and mode structure

Electromagnetic waves in a glass-fiber must be solutions to Maxwell's equations. The wave equation for the electric field obtained by rearranging Maxwell's equations, containing no free charges or currents reads

$$\Delta\vec{E}(\vec{r},t) - \mu(\vec{r})\epsilon(\vec{r})\frac{\partial^2\vec{E}(\vec{r},t)}{\partial t^2} = 0, \tag{1.1}$$

where $\mu(\vec{r})$ and $\epsilon(\vec{r})$ are the permittivity and permeability and characterise the response of the material to electric and magnetic fields.

We are interested in propagating waves along the fiber, where z points in the direction of propagation. One can write the components of the electric field $\vec{E}(\vec{r},t)$ and the magnetic field $\vec{H}(\vec{r},t)$ propagating along the fiber in cylindrical coordinates as

$$\begin{bmatrix}\vec{E}(\vec{r},t)\\ \vec{H}(\vec{r},t)\end{bmatrix} = \begin{bmatrix}\vec{E}(r,\varphi)\\ \vec{H}(r,\varphi)\end{bmatrix}\exp(i[-\omega t + \beta z]). \tag{1.2}$$

Here, $\omega/2\pi$ is the frequency of an optical wave in the medium and β is the propagation constant of the light in the medium. By plugging these equations into the wave equation and making use of Maxwell's equations, all field components can be derived from the z-components of the electric and magnetic field. The wave equation yields

$$\left[\partial_r^2 + \frac{1}{r}\partial_r + \frac{1}{r^2}\partial_\varphi^2 + (k^2 - \beta^2)\right]\begin{bmatrix}E_z(r,\varphi)\\ H_z(r,\varphi)\end{bmatrix} = 0, \tag{1.3}$$

which can be separated into a radial part and an azimuthal factor of $\exp(\pm il\varphi)$. The radial dependence of the axial field components of Eq. (1.3) yields

$$\left[\partial_r^2 + \frac{1}{r}\partial_r + (k^2 - \beta^2 - \frac{l^2}{r^2})\right]\begin{bmatrix}E_z(r)\\H_z(r)\end{bmatrix} = 0. \tag{1.4}$$

Solutions of fiber guided modes

Eq. (1.4) can be solved via modified Bessel functions for boundary conditions given by the wave vector $k = n\omega/c$. Note that the refractive index changes abruptly at the core-cladding boundary. By choosing an appropriate ansatz for the wave along the core and in the cladding one finds the following eigenequation

$$\left[\frac{J_l'(ha)}{haJ_l(ha)} + \frac{K_l'(qa)}{qaK_l(qa)}\right]\left[\frac{n_1^2 J_l'(ha)}{haJ_l(ha)} + \frac{n_2^2 K_l'(qa)}{qaK_l(qa)}\right] = \left[\frac{1}{(qa)^2} + \frac{1}{(ha)^2}\right]^2\left[\frac{l\beta}{k_0}\right]^2, \tag{1.5}$$

where J_n and K_n denote the Bessel functions and their derivatives J_n' and K_n'.

In this notation, the definitions $h = (n_1^2k^2 - \beta^2)^{1/2}$ and $q = (\beta^2 - n_2^2k^2)^{1/2}$ define the transverse wave number of the guided mode in the core and the cladding, respectively, a is the fiber radius, and k_0 is the wave number in vacuum. Solving this equation for the eigenvalues of β allows for the derivation of the mode profile functions $e_r(r), e_\varphi(r), e_z(r), h_r(r), h_\varphi(r)$, and $h_z(r)$. One possible solution for the profile function is a quasi-circularly[1] polarized mode, that can be written as

$$\vec{e}^{(\omega fl)} = \hat{r}e_r^{(\omega fl)} + \hat{\varphi}e_\varphi^{(\omega fl)} + \hat{z}e_z^{(\omega fl)} = \hat{r}e_r + l\hat{\varphi}e_\varphi + f\hat{z}e_z. \tag{1.6}$$

Here, $\hat{r}, \hat{\varphi}$ and $\hat{z}$ are the unit basis vectors of the cylindrical coordinates and ω, f and l define the mode: where ω is the mode frequency, f denotes the direction of propagation ($+$ or $-$) and l denotes the direction of circular polarization ($+$ or $-$). Plugging the mode function back into the ansatz for the propagating wave yields

$$\vec{E}_{\text{circ}}^{(\omega fl)} = A(\hat{r}e_r + l\hat{\varphi}e_\varphi + f\hat{z}e_z)\mathrm{e}^{if\beta z + il\varphi}, \tag{1.7}$$

assuming $e_r(r), e_\varphi(r), e_z(r)$ to be dimensionless, where the coefficient A is determined by the power of the field. Another solution for the profile function is a quasi-linear polarized mode, that is the superposition of two quasi-circular polarized modes with

[1] The term "quasi" arises since there are non-negligible fields in z direction

counter circulating polarization. This yields

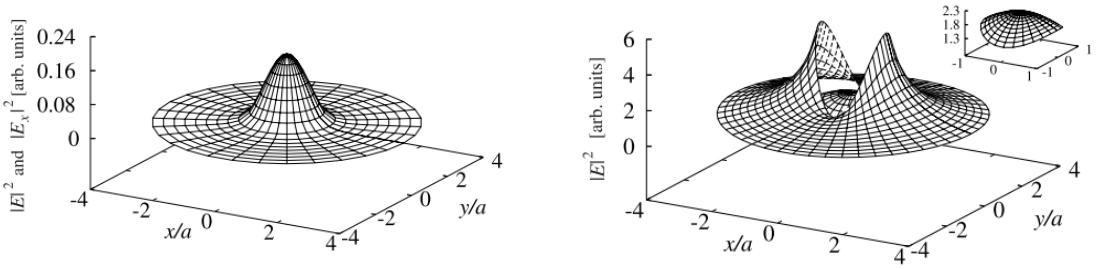
$$\vec{E}_{\text{lin}}^{(\omega f \varphi_0)} = \frac{1}{\sqrt{2}}(\vec{E}_{\text{circ}}^{(\omega f +)} \mathrm{e}^{-i\varphi_0} + \vec{E}_{\text{circ}}^{(\omega f -)} \mathrm{e}^{+i\varphi_0}). \tag{1.8}$$

The angle φ_0 denotes the polarization angle in the plane perpendicular to z, where $\varphi_0 = 0$ and $\varphi_0 = \pi/2$ corresponds to the x and y axis, respectively. Substituting the expressions for quasi-circular polarized light into this equation leads to the expression

$$\vec{E}_{\text{lin}}^{(\omega f \varphi_0)} = \sqrt{2}A\left[\hat{r}e_r \cos(\varphi - \varphi_0) + i\hat{\varphi}e_\varphi \sin(\varphi - \varphi_0) + f\hat{z}e_z \cos(\varphi - \varphi_0)\right] \mathrm{e}^{if\beta z}. \tag{1.9}$$

The expressions for the magnetic mode profile can be derived analogously.

As one can see in Fig. 1.3, the intensity distributions in a standard optical fiber and a nanofiber are exceedingly different. In Fig. 1.3a the intensity $|E|^2$ is symmetric and decays continuously. In a nanofiber (Fig. 1.3b) guiding quasi-linear polarized light, the cylindrical symmetry is broken, where the intensity maxima are aligned along the polarization of the guided light. Additionally the field intensity has a conspicuous discontinuity at the fiber surface.



(a) (b)

Fig. 1.3 Intensity distribution of the electric field of a linear polarized HE_{11} mode for $\lambda = 1300\,\mathrm{nm}$. a) standard glass fiber with a radius of $4\,\mu\mathrm{m}$, $n_1 = 1.4469$ and $n_2 = 1.4419$. b) nanofiber with a fiber diameter of $0.4\,\mu\mathrm{m}$ and $n_1 = 1.4469$. Note that the evanescent field in the nanofiber is not azimuthally symmetric. Taken from Le Kien et al. (2004b).

Mode spectrum of guided light

Now taking into consideration the eigenvalues of β, one can separate the mode profiles into HE_{lm} and EH_{lm} modes, where l corresponds to the mode number and m counts the solutions of β for increasing values of ha (product of core-guided field and radius of the core). HE or EH denotes which of the dimensionless z-components is larger

(e.g. $e_z > h_z \rightarrow EH$). For a fiber-based dipole trap it is convenient to have only a single guided mode. The quantity $V = ka\sqrt{n_1^2 - n_2^2}$, also known as the normalized frequency, determines how many modes can propagate in the nanofiber. For fibers where $V < 2.405$ only the HE_{11}-mode can form.

1.2.2 Dipole interaction and dipole trapping

Dipole traps are a very prominent way of trapping neutral atoms with light. The origin of the trapping potential can be derived by a semi-classical approach of a two-level-atom interacting with an external light field. Below, the results of a complete derivation as seen in Foot (2004) and Grimm and Ovchinnikov (1999) are outlined.

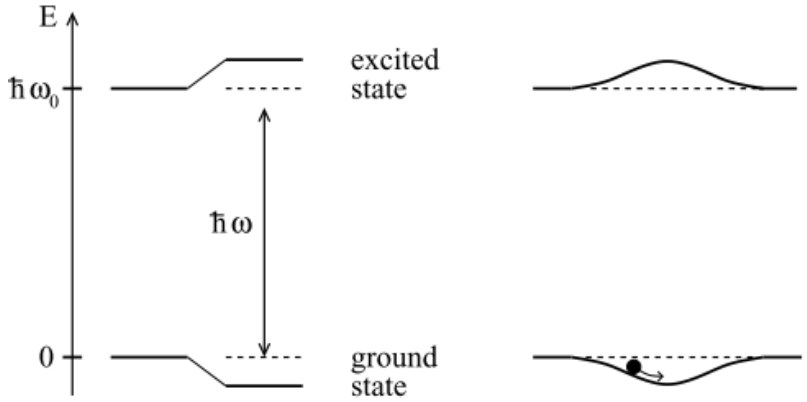


Fig. 1.4 (left) Scheme of a two-level atom modelled by a ground and an excited state with an energy difference of $\hbar\omega$. (right) A red-detuned light field leads to splitting of the energy levels, which can form a state dependent attractive or repulsive potential. Taken from Grimm and Ovchinnikov (1999).

A two-level atom consists of two energy eigenstates of the atomic Hamiltonian, i.e. a ground state $|g\rangle$ and an excited state $|e\rangle$ with an energy difference of $E = \hbar\omega$ (Fig. 1.4). Under the assumptions of no charges and currents close to the atom and an external field with a wavelength longer than the approximate dimension of an atom ($\vec{k} \cdot \vec{r} \ll 1$), where $\vec{r}$ corresponds to the atomic extension, the interaction potential between the field and the electron reads

$$H_{int} = -\vec{d} \cdot \vec{E}, \tag{1.10}$$

with the external electric field

$$\vec{E} = \epsilon\, \hat{e}\, \mathrm{e}^{-i\omega t} + \text{c.c.} \tag{1.11}$$

Here we use the dipole moment $\vec{d} = -e\vec{r} = \epsilon_0 \chi_\alpha \vec{E}$, where $\hat{e}$ is the unit vector of the polarization, ϵ is the amplitude of the external field, e is the electronic charge and $\epsilon_0 \chi_\alpha = \alpha$ is the polarizability of the atom. An interaction potential for an induced dipole can be derived via time averaging (note the factor 1/2) and is given by

$$U_{\text{int}} = \frac{1}{2}\epsilon_0 \chi_\alpha E^2 = \frac{1}{2}\langle e\vec{r}\vec{E}\rangle, \tag{1.12}$$

where $\langle\cdot\rangle$ denotes a time average. Using optical Bloch equations to derive the time average of an induced dipole in a two-level atom yields

$$U_{\text{dip}} = \frac{\hbar\Gamma}{8}\frac{\Gamma}{\delta}\frac{I}{I_{\text{sat}}}, \tag{1.13}$$

where I_{sat} is the saturation intensity

$$I_{sat} = \frac{\pi}{3}\frac{hc}{\lambda^3 \tau}\ . \tag{1.14}$$

In this notation, $\delta = \omega - \omega_0$ denotes the detuning of the laser frequency ω from the atomic resonance ω_0, $\tau = \Gamma^{-1}$ is the lifetime, and Γ the spontaneous emission rate of the excited state. The spontaneous emission enters the Bloch equations phenomenologically and can be derived to be

$$\Gamma = \frac{\omega_0^3}{3\pi\epsilon_0 \hbar c_0^3}|\langle e|\vec{d}|g\rangle|^2 \tag{1.15}$$

(see Grimm and Ovchinnikov (1999)). The resulting force of the light field acting on the atom depends on the sign of the detuning δ. When a field red detuned from resonance ($\omega < \omega_0$) is used, the atom is attracted towards the region of maximum intensity, whereas for blue-detuned light ($\omega > \omega_0$) the atom is repelled. The depth of the potential is proportional to I/δ, while the scattering rate of absorbed photons by the atom can be shown to be proportional to I/δ^2. Therefore very far detuned light fields of high intensities form reasonable traps. Conventional dipole traps typically use strongly focused red detuned lasers with high intensities to trap atoms around the focus of the light field. The big advantage of a nanofiber is that due to the strong confinement and guiding of the evanescent modes, large trapping regions along the fiber can be achieved. This makes the nanofiber a very useful device to trap atoms.

1.2.3 Geometry of the Nanofiber trap

The experiment presented in the outline of this thesis will be trapping Cesium atoms. To do so, a certain trapping configuration is needed to confine the atoms in three dimensions in close vicinity of the fiber. Additionally, it is planned to use trapping fields that lead to state-insensitive trapping. The experimental details as well as the desired configuration will be presented below.

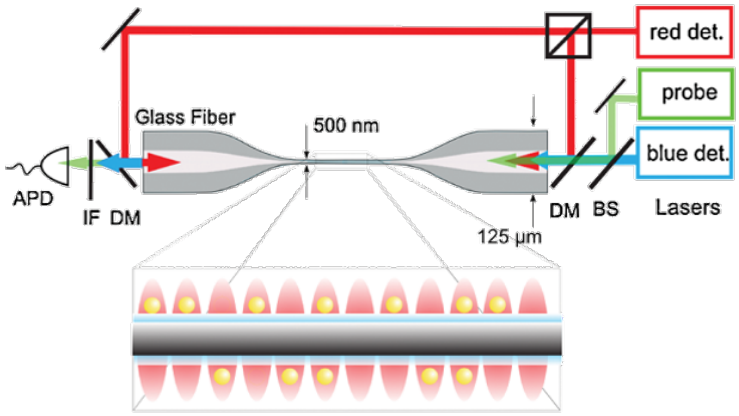


Fig. 1.5 Scheme of the experimental implementation of the nanofiber trap. The sketch shows the superimposing of the blue and red detuned trapping lasers as well as a probe laser via beamsplitters (BS) and dichroic mirrors (DM). For detection of the transmitted probe light, an avalanche photo diode (APD) is put at the output of the nanofiber after an interference filter (IF), to filter out the trapping fields. The zoomed region shows atoms loaded into the dipole trap. Taken from (Vetsch et al. (2010))

The aim of the guided trapping fields is to form a lattice of dipole traps on two opposite sides of the nanofiber, as sketched in Fig. 1.5. Additionally, resonant probe light is coupled into the fiber to determine the number of trapped atoms and perform experiments such as EIT and light storage. For the experimental implementation, the required fields need to be carefully aligned and overlapped using dichroic mirrors before being coupled into the nanofiber. The evanescent field around the nanofiber creates a dipole interaction for atoms close by, where a red detuned field propagates through the fiber and strongly attracts atoms. As one can see in Fig. 1.6b the intensity increases towards the fiber surface and atoms would be attracted towards the fiber. This, and additional van-der-Waals forces acting on atoms in close vicinity of the fiber, lead to collisions with the surface and therefore scattering or adsorption, preventing atoms from being loaded stably into a trapping site. To prevent the loss of atoms, a second force which repels the atoms from the fiber surface is needed, such as a blue-detuned field, superimposed with the red-detuned light. As one can derive from the mode

functions of the guided light in the fiber, the intensity of blue detuned light decays faster than the red-detuned light, so the resulting radial potential, after overlapping these two fields, has a local minimum, sufficient for radial trapping. This minimum is typically located approximately 200 nm above the fiber surface (see Fig. 1.6b).

To trap the atoms along the z-axis, the red laser is divided into two counter-propagating beams to create a standing wave in the fiber. To guarantee trapping in azimuthal direction, the distinct form of the quasi-linear HE_{11}-mode (see Fig. 1.3b) comes to use. Figure 1.6a shows the red- and blue-detuned fields propagating as quasi-linear modes with perpendicular polarization ($\Delta\varphi = \pi/2$). The overall trapping potential potential is shown in Fig 1.6d, oriented such that there are potential minima on opposite sides of the fiber, and the atoms are radially, longitudinally and azimuthally confined. This is the standard trapping configuration for nanofibers used in the group. Note that different combinations of polarizations, orientation of polarization and running and standing waves can create different trapping geometries or optical waveguides for atoms (Reitz and Rauschenbeutel (2012)). Experimentally it was shown that trapping Cesium atoms in this nanofiber-based dipole traps is possible and the ground state coherence properties of trapped Cesium are suitable for quantum-optical experiments with applications in quantum information processing (Reitz et al. (2013)).

Experimental implementation

In this experiment the dipole trapping fields are detuned with respect to the D2-line, which is at $\lambda_0 = 852\,\text{nm}$. The trapping fields use "magically" detuned wavelengths of $\lambda_{\text{red}} = 935\,\text{nm}$ and $\lambda_{\text{blue}} = 685\,\text{nm}$. Magic wavelengths minimize the induced light shifts of the $|F, m_F\rangle$ states of the D2-transition, allowing for state insensitive trapping via dipole interaction (Le Kien et al. (2004a)). The fiber radius was optimized, yielding a maximum in intensity for fixed guided power of the relevant wavelength to probe and manipulate the atoms, i.e. 852 nm. Previous calculations showed, that for a radius of $a \approx 0.23\lambda$ the intensity has a maximum on the fiber surface, but for an assumed trapping distance of 200 nm the optimal fiber radius for strong interactions with the atoms would yield roughly 170 nm. Unfortunately for this nanofiber geometry it might be more difficult to have low losses, and it might be difficult to achieve sufficiently deep traps. Further calculations for a fixed red trap power of 0.4 mW yield, that the fiber radius that maximizes the intensity at the position of the atoms is roughly the same as the one that maximizes the trap depth, i.e. 200 nm. This radius was chosen to use for the nanofiber put into the vacuum chamber, resulting in trapping of atoms at approximately 225 nm above the fiber surface. For this configuration, laser powers

of $P_{\mathrm{red}} = 0.4\,\mathrm{mW}$ and $P_{\mathrm{blue}} = 30\,\mathrm{mW}$ are derived to form sufficient dipole traps. For choosing the right fiber, several commercially available optical glass fibers have been tested for suppression of higher ordered modes than the HE_{11}-mode, for being single mode at all relevant wavelengths. Additionally, the magnitude of losses due to bending was measured for the trapping light fields. The best performing fiber, a Thorlabs SM800 could be successfully put in the vacuum chamber and tested to sustain 50 mW of fiber guided blue trapping light.

As one can see in Fig. 1.6b, typical two-colour dipole traps have a depth of only a few tenths of millikelvin. Therefore atoms must be already very cold to be actually trapped in the potential minima. Otherwise, they would have too much kinetic energy and just scatter and leave the trapping site again. To pre-cool the Cesium atoms and increase the probability of being trapped by confining them to a region close to the fiber, a magneto-optical trap (MOT) and optical molasses cooling will be used.

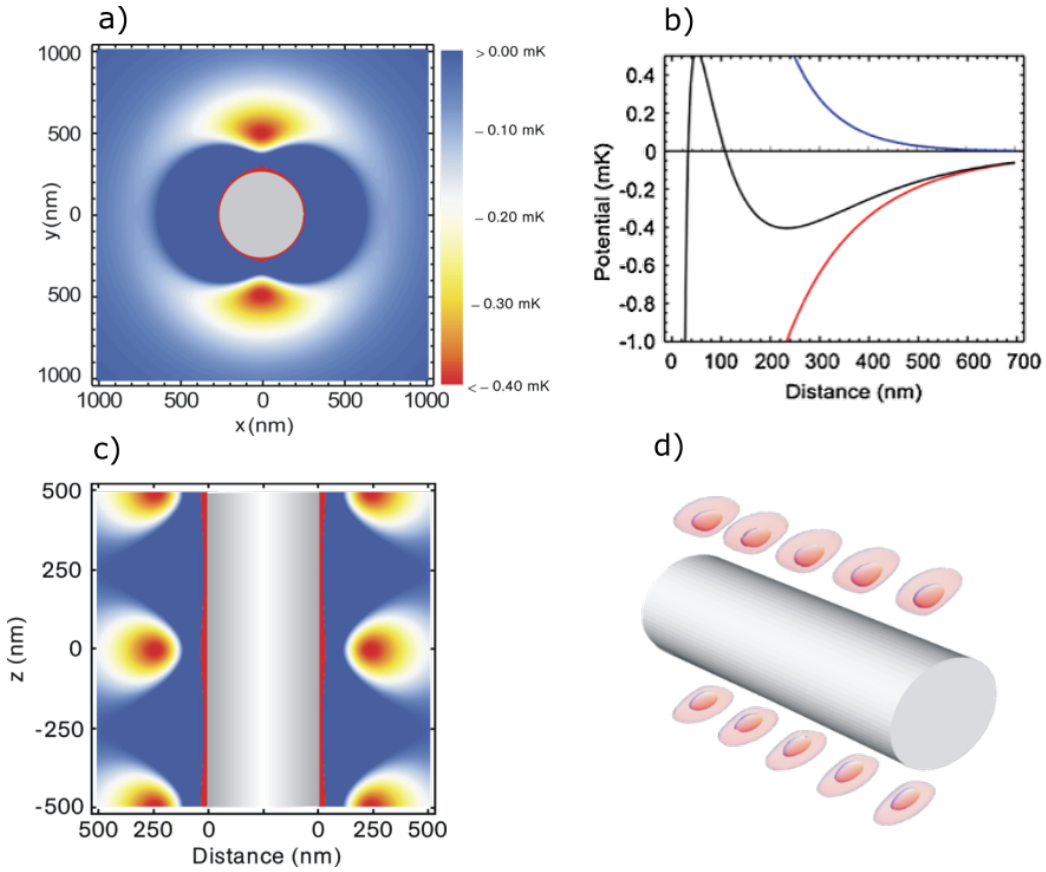


Fig. 1.6 Numerical calculations for an established nanofiber trap of the group for wavelengths of 780 nm and 1064 nm. a) Azimuthal trapping is obtained by overlapping two perpendicular quasi-linear polarized fields. The intensity distribution of the guided modes (Fig. 1.3b) add up such, that the induced dipole potential has minimaon two sides of the fiber. b) Radial dipole potential. The blue detuned repelling light decays faster than the red detuned attractive field. This way a radial trapping potential (black) is formed. For very low distances van-der-Waals forces act strongly attractive. c) Longitudinal trapping is achieved by creating a standing wave in the nanofiber via two counter-propagating red-detuned lights. d) shows a 3D rendering of the dipole traps with equipotential surfaces at 40 µK and 125 µK. Taken from Vetsch et al. (2010).

Chapter 2

Cooling setup

The nanofiber trap will be the backbone of this experiment and can trap Cesium atoms along the nanofiber, allowing manipulation of their internal states. The dipole traps created in close vicinity of the fiber surface are only a fraction of a millikelvin deep. The atoms must be cooled right next to the nanofiber so they can be loaded into the traps without being scattered right away. To do so, an optically dense cloud of cold atoms is formed via magneto-optical-trapping (MOT) and then further cooled in an optical molasses. The particularity about this experiment is that it is planned to have a strongly elongated cigar shaped MOT. Establishing this MOT-configuration requires the overlapping of six laserbeams with an appropriate intensity distribution among them, intersecting at the center of a magnetic quadrupole field. In this chapter I will discuss the theoretical basis of laser cooling of atoms and describe the experimental cooling setup.

2.1 Preparation of Cesium atoms for loading into dipole traps

2.1.1 Trapping and cooling the atoms

Atoms can be cooled via momentum transfer from light to the atom and back by absorbing and re-emitting photons. The total momentum is conserved during this interaction, so whenever an atom absorbs a photon it gets a recoil kick $\hbar k$ proportional to the photons wavevector k. Repeatedly absorbed photons will be re-emitted spontaneously into any direction, which also transfers momentum respectively. This results in a net force equal to the number of scattered photons given by the scattering rate

and the transferred momentum per photon

$$F_{\text{scatt}} = \hbar k R_{\text{scatt}} \ . \tag{2.1}$$

The scattering rate $R_{\text{scatt}} = \Gamma\rho_{22}$ can be derived from the optical Bloch equations by multiplying the population of the excited state ρ_{22} with the decay rate for spontaneous emission Γ, which yields

$$R_{\text{scatt}} = \frac{\Gamma}{2} \frac{I/I_{\text{sat}}}{1 + I/I_{\text{sat}} + 4\delta^2/\Gamma^2} \ , \tag{2.2}$$

where I_{sat} is the saturation intensity and δ is the detuning (see Foot (2004)). As one can see, the scattering rate, and therefore the scattering force, depends on the detuning δ, which is the difference between the wavelength for a resonant transition and the wavelength used to excite the atom. For a moving atom, the detuning arises due to the Doppler-effect. As shown in Fig. 2.1, the absorption of a photon, when moving towards a counter-propagating laser, is most probable if the velocity of the atom results in a Doppler shift that shifts the frequency seen by the atom back on resonance. Therefore red-detuned lasers are necessary to slow down an atom. Re-emission of the absorbed photon in any direction and repetition of this process over many times actively cools the atom.

Optical molasses

Due to the Doppler effect the force acting on the atom differs according to the direction of motion of the atom. An easy explanation can be given for a two-level atom moving to the right, interacting with two counter-propagating red-detuned beams coming from left and right. As one can see in Fig. 2.1, the Doppler effect shifts the wavelength seen by the atom towards resonance for the beam propagating to the left, which leads to a higher probability of scattering, while the exact opposite happens for the beam propagating to the right. This can be written as a net-force along this axis as

$$F_{\text{mol}} = F_{\text{scatt}}(\omega - \omega_0 - kv) - F_{\text{scatt}}(\omega - \omega_0 + kv) \approx -2\frac{\partial F_{\text{scatt}}}{\partial \omega} kv = -\alpha v \ , \tag{2.3}$$

where the first and second terms denote the contribution of the beams propagating to the right and left, respectively. Note that $\omega - \omega_0$ is the detuning from resonance and kv comes from the frequency shift of the Doppler effect. The equation can be written introducing α as a damping constant, which is why this technique is called optical

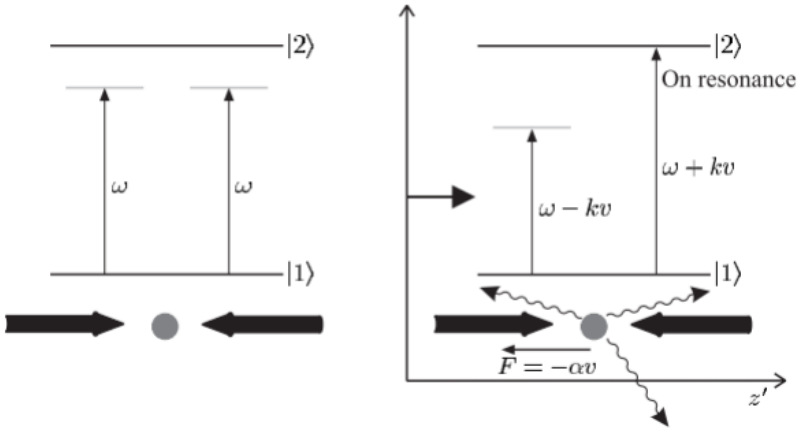


Fig. 2.1 (left) An atom resting between two counter-propagating fields experiences no net force since the scattering rate for both directions is the same. (right) If the atom moves in one direction the Doppler-effect shifts the frequency of one laser towards resonance, so the scattering increases and the atom experiences a net force in opposite direction. Taken from Foot (2004).

molasses. When only low velocities ($kv \ll \Gamma$) are considered, α can be derived from the scattering force

$$\frac{\partial F_{\text{scatt}}}{\partial \omega} = \frac{\hbar}{c}(R_{\text{scatt}} + \omega \frac{\partial R_{\text{scatt}}}{\partial \omega}), \tag{2.4}$$

to be

$$\alpha = 4\hbar k^2 \frac{I}{I_{\text{sat}}} \frac{-2\delta/\Gamma}{[1 + 4\delta^2/\Gamma^2]^2} \ . \tag{2.5}$$

Consideration of fluctuations in the spontaneous emission and absorption of photons which both lead to heating of the atoms, allows an estimation of the lowest possible temperature of the atomic cloud, cooled in counter-propagating beams. This so-called Doppler temperature can be written as

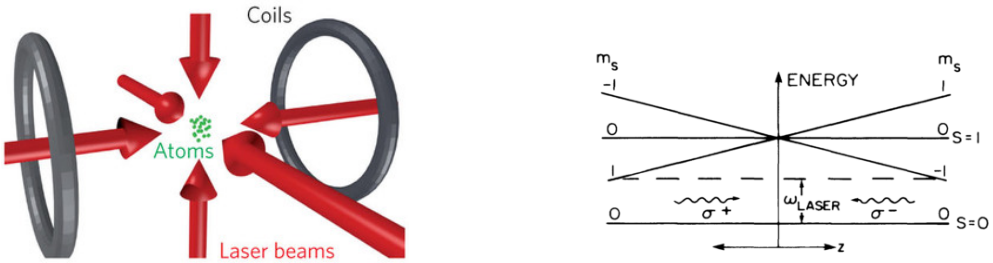
$$k_{\text{B}} T_{\text{D}} = \frac{\hbar\Gamma}{2}, \tag{2.6}$$

and is 125.61 µK for the Cesium D2-line (Steck (2008)). To cool atoms efficiently, the overall kinetic energy has to be lowered, such that the velocities are reduced in all three dimensions, where one gets an effective cooling effect proportional to α. An easy way of doing so is shown in Fig. 2.2a, where six counter-propagating red-detuned laser beams along three perpendicular axes are meeting in one point, where essentially each beam slows the atom in one direction (Lett et al. (1989)). The area of beam intersection, where atoms can be cooled in all three dimensions, is of finite size and atoms in the molasses can diffuse out of this area, due to their remaining velocity, therefore only

atoms below a certain velocity can be trapped sufficiently. Atoms that move to fast, will only remain in the molasses for short times and therefore experience no adequate cooling. For more efficient cooling, the atoms need to be confined to the intersection area of the lasers, which can be done with a magneto optical trap.

Magneto optical trap

To trap atoms in a magneto optical trap, one makes use of the splitting of degenerate atomic levels in a magnetic field, called Zeemann splitting, in combination with appropriately polarized light, to create a position dependent force towards the trapping centre. In a magnetic field, degenerate atomic energy levels split into sub-levels, according to their projection m_J of the angular momentum along a specified axis. As seen in Fig. 2.2b, the energy levels vary linearly with the position of the atom with respect to the centre of a magnetic quadrupole field, with a field gradient along the z-axis. In this direction, the field is pointing away from the centre $z = 0$, where the B-field is zero and the energy levels remain degenerate. Note that for x and y direction the field points towards the centre. Looking at the MOT along the z-axis (Fig. 2.2b), atoms to the right of the magnetic field centre ($z > 0$) can be excited via red-detuned light, which is σ_--polarized with respect to the atomic transition. The same occurs for atoms on the left ($z < 0$) for reversed properties of all parameters. For theoretical



(a) (b)

Fig. 2.2 a) Scheme of a typical MOT setup. Three pairs of counter-propagating lasers with circular-polarized light intersect in a point where the magnetic quadrupole field is zero. Taken from Estève (2013). b)The magnetic field leads to a position dependent splitting of the m_J-states (here m_S). Suitable circular polarized light can excite the atom and effectively push it back towards the centre via scattering of photons. Taken from Raab et al. (1987).

calculations, the energy splitting induced by the Zeeman effect, dependent on the

B-field, needs to be considered in Eq. (2.4). This yields

$$F_{\mathrm{MOT}} = F^{+}_{\mathrm{scatt}}(\omega - kv - (\omega_0 + \beta z)) - F^{-}_{\mathrm{scatt}}(\omega + kv - (\omega_0 - \beta z)), \tag{2.7}$$

with F^+ and F^- being the scattering forces induced by $\sigma+$ and $\sigma-$ transitions, respectively. The force acting on the atom is now both velocity and position dependent. For ($kv \ll \Gamma$) this equation can be approximated to be

$$F_{\mathrm{MOT}} \approx -2\frac{\partial F_{\mathrm{scatt}}}{\partial \omega} kv + 2\frac{\partial F_{\mathrm{scatt}}}{\partial \omega_0}\beta z, \tag{2.8}$$

The term $\omega_0 + \beta z$ is resonant for $\Delta m_J = +1$ transitions at the position z and $\omega_0 - \beta z$ is resonant to $\Delta m_J = -1$, accordingly. This can be re-written as

$$F_{\mathrm{MOT}} = -2\frac{\partial F}{\partial \omega}(kv + \beta z) = -\alpha v - \frac{\alpha\beta}{k} z, \tag{2.9}$$

where the position dependent force acts similar to a spring constant, given by

$$\beta z = \frac{g\mu_{\mathrm{B}}}{\hbar}\frac{\mathrm{d}B}{\mathrm{d}z} z, \tag{2.10}$$

with g as the Landé-factor and μ_{B} is the Bohr magneton. As one can see, atoms moving away from the centre are actively pushed back towards the centre due to a higher probability of scattering. Using appropriate polarized light for the other two directions allows for cooling and trapping atoms. With this additional trapping mechanism, i.e. the position dependent term of the scattering force, the atoms remain longer in the intersection area of the beams. Therefore, cooling and trapping of atoms with higher initial velocities is possible and pre-cooling atoms to load a MOT is not necessary.

Subsequent cooling

After trapping, the magnetic field will be turned off and further cooling in an optical molasses will be performed to dissipate kinetic energy, allowing for trapping atoms in the nanofiber based dipole trap. After the MOT-stage, the atoms see light from counter-propagating differently circular polarized light. The approach, given in section 2.1.1, is not suitable to describe the full dynamics of the atom, interacting with polarized light fields. The standing waves created in the intersection region of the laser beams have a position depending polarization, and atoms moving along any direction in the atomic cloud see an according change in polarization. This leads to cooling mechanisms that allow for sub-Doppler temperatures, which is theoretical discussed in Dalibard and

Cohen-Tannoudji (1989). The theoretical temperature minimum, that can be achieved by this cooling technique, is called recoil temperature, and is given by

$$k_B T_{\mathrm{rec}} = \frac{\hbar^2 k^2}{M}, \tag{2.11}$$

which is 193.34 nK for Cesium (Steck (2008)).

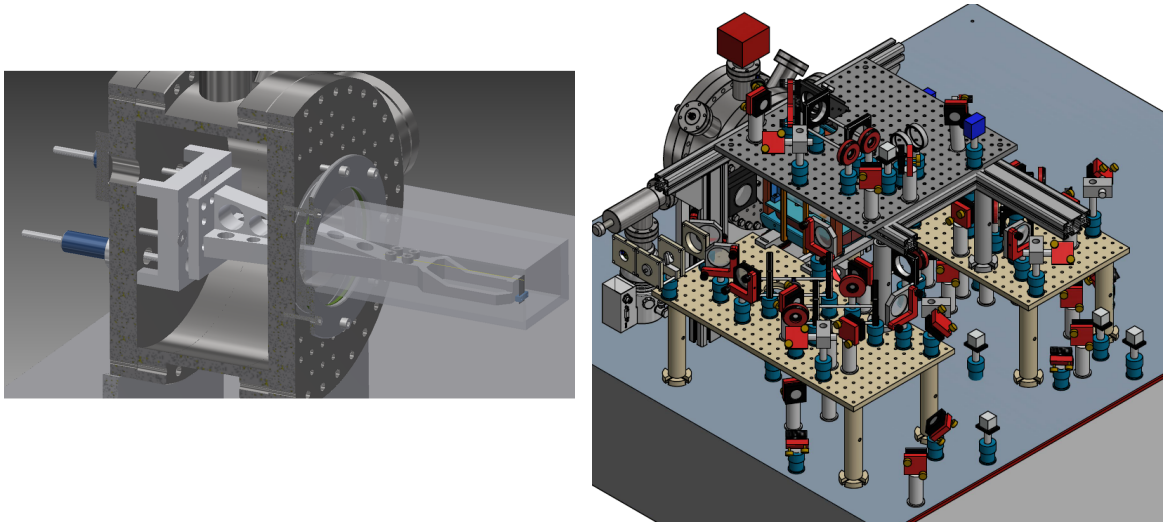
2.2 Experimental implementation

In the experiment, the setup for the MOT and optical molasses consists of three pairs of counter-propagating circular polarized laser beams, intersecting in the centre of a magnetic quadrupole field. For creation of an appropriate field and compensation of background, three coil pairs are mounted in a cage system closely around the glass cell. The beam crosssection is elliptical, to be able to form a strongly elongated MOT and the laser beams are carefully balanced and stabilized regarding their intensity. In this section I will outline the experimental details of the implementation of the MOT setup, discussing how the MOT-beams are distributed and aligned, as well as give a summary of the proposed experimental conditions.

Experimental outline

The experiment consists of a vacuum chamber with an attached glass cell. As one can see in Fig. 2.3a, in the camber, there is an aluminium arm mounted on the back-flange of the chamber reaching into the glass cell, free to tilt around two axes to position the fiber holder attached to its front end, where the fiber is glued. The glass cell allows for great optical access, since the inside is visible from all sides except for the one where it is mounted. A cage holding the magnetic coils is put over the glass cell in very close vicinity.

The glass, mounted onto the chamber, rests at a height of approximately 30 cm and beams that will enter the cell need a suitable construction to host the optical setup at the same height. This is done via a breadboard construction (see Fig. 2.3b), where two boards are put on posts to the left and right of the cell, and a third board is put above the glass cell. Theses breadboards host the optical setup for the MOT-beam alignment, the imaging system and support the magnetic-coil cage construction. To suppress possible vibrations in the setup, that might influence the optical alignment, the lower two breadboards rest rigidly on several randomly placed columns, to avoid any symmetrical vibrational excitation. Additionally, thick quadratic steel plates were



(a) (b)

Fig. 2.3 a) The fiber-mount is attached to a tiltable arm, to position the glass fiber glued on it with respect to the MOT-cloud. b) Construction of the breadboard setup to host the MOT-beam alignment and imaging setup.

glued on the back of the boards with thick double sided adhesive bands to efficiently dampen oscillations. For the upper breadboard a massive support, consisting in several aluminium braces, was rigidly mounted to the breadboard. The whole construction is connected to the experimental table, that floats on air cushions and is constructed in a way to dampen vibrations effectively.

The atomic cloud in the MOT is planned to be strongly elongated and cigar shaped, oriented along the fiber axis, with a desired diameter of about 1 mm and a length of 10 mm. To achieve this, two perpendicular pairs of counter-propagating beams will confine the cloud horizontally and another pair, coming from the top breadboard and the optical table will confine the atoms vertically. Note that for forming the desired shape of the cloud, the beam crosssection has to be elliptical and oriented appropriately, which is why the vertical beams need to have higher laser intensities, to stronger confine the cloud.

For the cooling of Cesium atoms, the hyperfine splitting of the D2-line is used. As sketched in Fig. 2.4, the $F = 4$ to $F' = 5$ transition is used as cooling cycle and the transition $F = 3$ to $F' = 4$ is needed to pump atoms, that decay into the lowest ground state back to take part in the cooling cycle. For this procedure, two lasers called “Cooler” and “Repumper” are used, operated at wavelengths of approximately

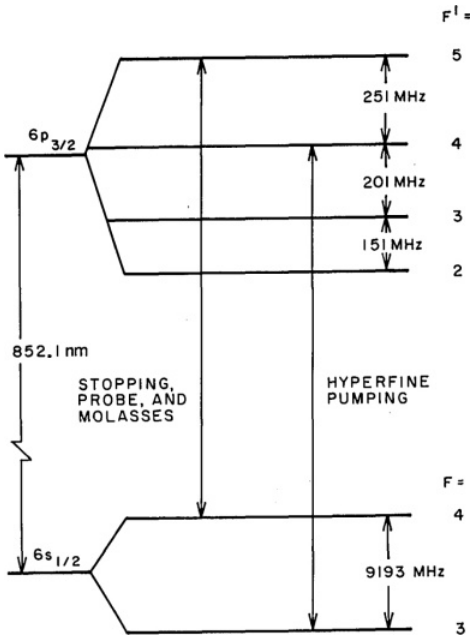


Fig. 2.4 Scheme of the Cesium D2-transition and hyperfine splitting. In our experiment we use the transition F=4 to F'=5 for cooling and F=3 to F'=4 to pump atoms that have decayed into the ground state back, so they can take part in the cooling cycle again. Taken from Sesko and Wieman (1989)

852 nm, detuned from each other by 9.19 GHz. The detunings and intensities can be fine-tuned with an acousto-optical modulator (AOM).

In our experiment the MOT is loaded with atoms at room temperature, present in the vacuum as background gas, since there will always be a sufficient amount of atoms, slow enough to experience scattering in the MOT. The Cesium can be brought into the vacuum via outgasing from a metallic dispenser, integrated in the vacuum chamber.

MOT-beam distribution

The beam distribution setup as shown in Fig. 2.5 first overlaps the Cooler and Repumper and then splits the combined beam into six arms, where the splitting is always done by a combination of a $\lambda/2$ waveplate and a polarizing beam splitter cube (PBS).

The combining of the lasers is done with a pair of mirrors, to overlap the two beams in both arms of the PBS. Subsequently, the waveplates are turned to only guide light in one arm. After that, the beam is split 50:50, into vertical and horizontal trapping beams. The horizontal arm needs to be split again twice, so the final four MOT-beams have 12.5% of the initial intensity (Top four beams in Fig. 2.5). The beams are then guided up to the lower breadboards, on which the final alignment takes place. The

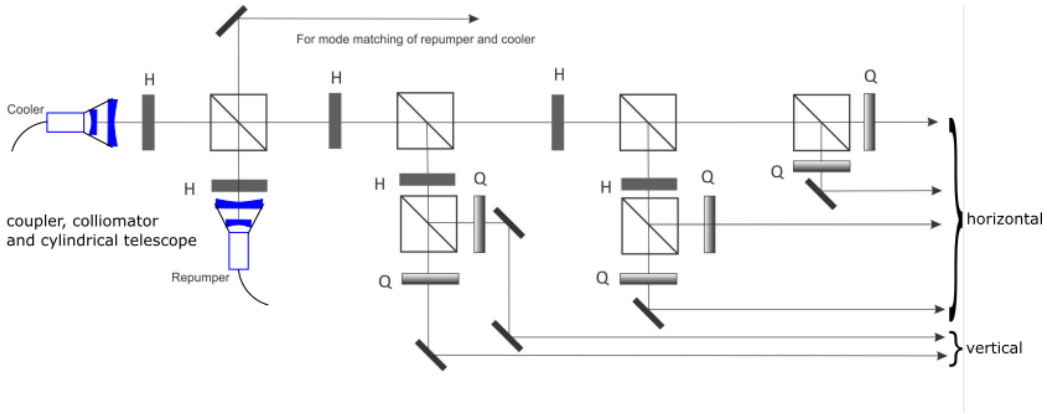


Fig. 2.5 The light coming from the laser is coupled and cylindrically shaped in the cage mounts, denoted in blue. After that, $\lambda/2$ waveplates (H) are used to match and split the beams in combination with polarizing beam splitters (cubes). To adjust a circular polarization, $\lambda/4$ waveplates (Q) are used. After distributing, the beams are guided to the breadboards, where they are widened and aligned.

vertical MOT-beams need stronger intensities, so the beam is split only once to have 25% of the initial intensity. One beam will be aligned on the optical table before guiding through the glass cell, while the other beam is guided to the top breadboard.

The mirrors implemented in the experiment have a slightly polarization-dependent reflectivity, so the beams having clean polarizations after passing the PBS, will have more losses induced by the mirrors in one arm than in the other one. To compensate for that behaviour, the waveplate in front of each PBS has to be positioned in a way, that the beams leave with slightly unbalanced intensities. In the end, the beam intensity distribution at the laser intersection area should be 12.5 to 25 for the horizontal to vertical beams, respectively, ultimately balanced correctly by determining the MOT shape and position, as well as the expansion behaviour of the optical molasses.

MOT-beam shaping

To shape the beam cylindrically, the fiber out-coupling of the Cooler and Repumper were put in a cage system together with a telescope consisting of 2 cylindrical lenses. In Fig. 2.7, one sees the beam shape of the widened and collimated beam, where one direction has been magnified by the telescope, while maintaining the size of the beam in the other direction. Note that a cylindrical telescope is prone to beam deformation, which is why, the lenses have to be centred carefully with respect to the passing beam and should not be tilted with respect to each other. A misaligned system can

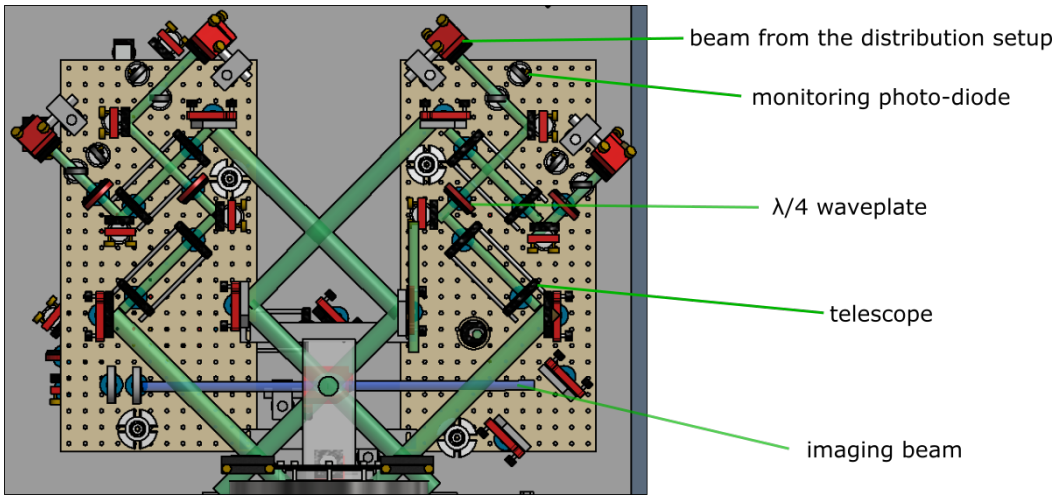


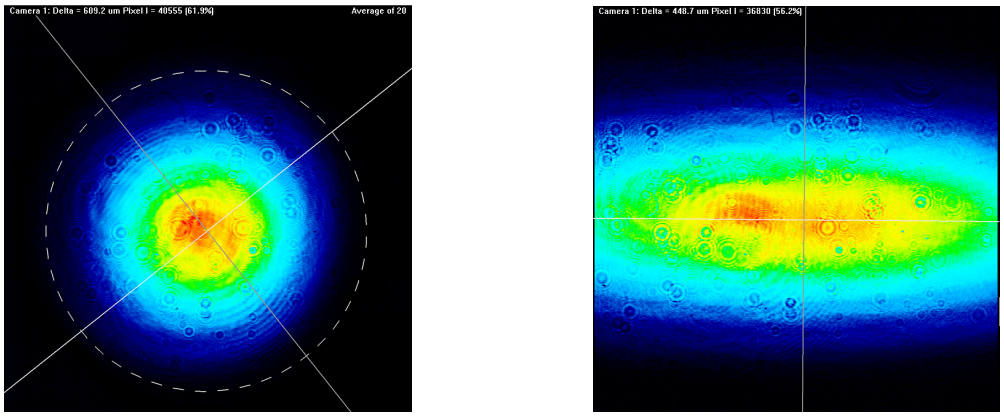
Fig. 2.6 Setup of the MOT-beam alignment on the lower breadboards. The beams, indicated in green, are aligned via a pair of mirrors, guided through a $\lambda/4$ waveplate and widened by a telescope. After that, another pair of mirrors guided the beams through the glass chamber at an angle of 45° with respect to the fiber axis. The horizontal imaging beam is indicated in blue.

be recognized if the shape of the beam changes over distance from cylindrical over barrel-shaped to cylindrical but perpendicularly oriented.

MOT-beam alignment

After distributing the beams, a setup is needed to further widen the beams and align them to overlap and counter-propagate at the intersection point as seen in Fig. 2.6. To do so, circular telescopes are placed into each beam line, yielding a magnification of 3.5. To achieve the cylindrical shape of the cloud, the horizontal beam pairs should pass each other perpendicularly with an angle of 45° with respect to the fiber axis. After passing the telescopes, the beams are guided through the small windows set by the magnetic coils to pass the glass cell at an angle. The vertical beams, which are also cylindrically shaped, are magnified and guided through the glass cell, from above and below. For the alignment 2 inch mirrors were used, placed in such a way, that the long axis of the elongated beam shape is oriented along the fiber axis for all 6 beams.

To monitor the MOT-beams, photo-diodes were put at suitable places behind mirrors that transmit sufficient light and where this was not possible, glass windows were put into the beam in a small angle, to reflect a portion of the beam onto a photo-diode. Additionally, the intensities of the Cooler and Repumper are stabilized



(a) (b)

Fig. 2.7 a) Beam shape of the cooling laser before entering the cylindrical telescope. b) After passing, the beam is stretched in horizontal direction, maintaining the vertical size. Note that the two pictures are to scale.

by connecting the output of the diode to a feedback loop, that controls the AOMs, to compensate for drifts and fluctuations in the laser intensity.

In the last step, the MOT-beams need to be polarized in a way, that a pair of counter-propagating beams is perpendicularly circular polarized, by placing $\lambda/4$ waveplates in front of the telescopes. The polarization was measured with a polarimeter and aligned before the vacuum chamber and the glass cell were put to its final destination.

Magnetic setup

For the magnetic setup, three pairs of coils have been wound on a compact cage (see Fig. 2.8), that fits tightly around the glass cell and leaves sufficient room for the MOT-beams to pass. The construction consist of a pair of so called "MOT" and "Bias" coils to form the required quadrupole field and a pair of compensation coils to compensate for earth's magnetic field. Each coil can be operated individually and be switched sufficiently fast to have a homogeneous field for Zeemann splitting, as required for further experimentation. The coils are designed to have a maximum of uniform field of about 120 Gauss, or a magnetic field gradient of 10 Gauss/cm with a ratio of 5 to 1 between the transverse and longitudinal gradient in MOT configuration.

Experimental parameters

In this experiment, the laser power of the Cooler has been calculated to be approximately 12 mW in the horizontal plane and 24 mW in the vertical direction, while detuned by

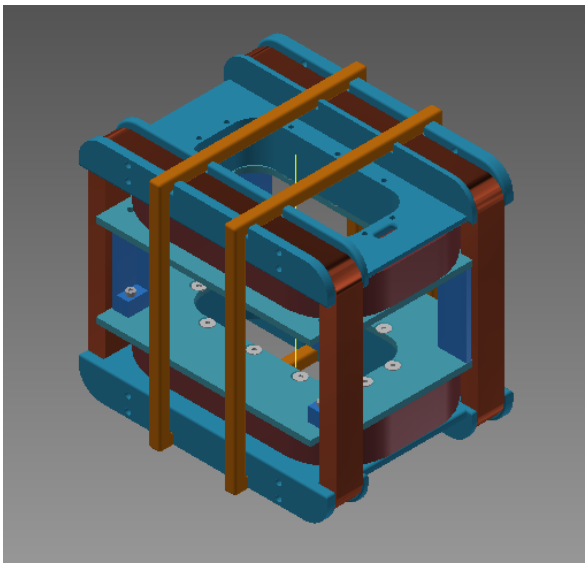


Fig. 2.8 Construction drawing of the magnetic coil setup. The inner, horizontally aligned pair is the MOT pair to create a magnetic field gradient perpendicular to their plane. The outer pair, is the Bias pair, to create a magnetic field gradient accordingly. The outermost pair is installed solely to create an homogeneous offset. Each coil can be operated individually to create the desired quadrupole or homogeneous field to operate the trap and compensate for the earths magnetic field at the same time.

15 MHz from resonance. This intensity corresponds to $24\, I_{\mathrm{sat}}$, which is necessary to have sufficient scattering due to the detuning dependency of the scattering rate Γ (see Eq. (2.3)). The Repumper will be operated with an intensity of about 1.5 mW.

For the subsequent cooling, the magnetic coils will be switched off and the detuning of the counter-propagating beams will be raised to approximately 75 MHz. This way, a significant amount of atoms can dissipate sufficient kinetic energy, to be loaded into the dipole traps. The success in doing so strongly depends on the careful alignment of the beam orientation, intensity and detuning. A final alignment can only be done on the running experiment, where absorption imaging can be used to characterise the MOT-cloud and expansion of the optical molasses.

Chapter 3

Absorption Imaging

The number of atoms and temperature achieved by laser cooling directly affect the efficiency of loading atoms into the nanofiber dipole trap. An appropriate implementation of an absorption imaging setup is needed to diagnose, optimize, and monitor the behaviour of the cooling process, i.e. the MOT and molasses. To this end, an attenuated resonant laser beam, sent through the atomic cloud is casting a shadow, that is imaged by an optical setup, projected onto a camera. Analysis of the acquired data delivers the desired parameters, such as shape, position, size, atom numbers and temperature of the cloud, allowing for optimization.

In this chapter I will discuss the theoretical details of absorbing light in an optically dense atomic vapour, introduce the fundamentals of optical imaging and outline the experimental implementation of the imaging setup.

3.1 Sensing atom-numbers and temperature of atom clouds

The atom-cloud is modelled as an optically dense vapour where a monochromatic resonant beam of light excites the atoms. Re-emission in random directions leads to an attenuation of the imaging beam and the transmitted intensity allows for calculation of the optical density and number of atoms in the cloud.

3.1.1 Absorption of light in optically dense atom vapour

Light going through an optically dense vapour of a length Δz sees $N\Delta z$ atoms per unit area on its way, where each atom could absorb light proportional to its absorption

cross-section σ. The attenuation of intensity of transmitted light can be written as $dI/dz = -\sigma N \Delta z$. Integration over d$z$ yields

$$I = I_0 e^{-N\sigma(\omega)z} = I_0 e^{-n\sigma(\omega)} = I_0 e^{-OD}, \tag{3.1}$$

which is known as Beer's Law. Note, that $Nz = n$ is referred to as the column density, which is the number of atoms in a infinitesimal thin column of height z. The absorption coefficient is defined as the scattered power divided by the incident flux

$$I\sigma = \hbar\omega R_{\text{scatt}}, \tag{3.2}$$

which yields by plugging in the scattering rate R_{scatt}

$$\sigma = \frac{\sigma_0}{1 + 4(\Delta/\Gamma)^2 + (I/I_{\text{sat}})}, \tag{3.3}$$

with

$$\sigma_0 = \frac{\hbar\omega_0\Gamma}{2I_{\text{sat}}} \tag{3.4}$$

(see Foot (2004)). Note that the saturation intensity I_{sat} is defined as the intensity, where the on-resonance scattering cross section $\sigma_0 = \sigma(\omega = \omega_0)$ multiplied with the population difference of excited and ground state atoms is 1/2. The often used expression I/I_{sat} can be derived from the steady state solution for the Bloch vector component w, which is the inversion or population difference, and yields

$$\frac{I}{I_{\text{sat}}} = \frac{2\Omega^2}{\Gamma^2}. \tag{3.5}$$

Experimentally, to determine the total number of atoms in the cloud, the optical density (OD) according to Eq. (3.1) is measured. Therefore three images have to be taken to determine the spatial resolution of the intensity of detected light. For the first picture an atomic cloud is present and light passing the vapour is attenuated to be I_{atoms}. The second picture is taken without atoms, defining the distribution of the imaging beam I_{img}. Finally, a picture for I_{dark}, without light and atoms is taken to compensate for the background (e.g. scattered light) and thermal noise of the camera. The measured optical density can be determined as

$$OD_{meas} = ln\frac{I_{\text{img}} - I_{\text{dark}}}{I_{\text{atoms}} - I_{\text{atoms}}}\ . \tag{3.6}$$

In absorption imaging there are two known systematic errors for which we have to account for. These are the saturation of the optical density and intensity saturation of the probe light (Lewandowski et al. (2003)). The first effect arises from light which is not sufficiently absorbed by the atoms, detected by the camera and therefore mimicking a lower measured OD. This can be caused by off-resonant or direct and indirect scattered light of the imaging beam. Due to this effect, it is not possible to measure ODs higher than the saturation optical density OD_{sat}. The optical density has to be modified via

$$OD_{\mathrm{mod}} = ln\frac{1 - e^{-OD_{\mathrm{sat}}}}{e^{-OD_{\mathrm{meas}}} - e^{-OD_{\mathrm{sat}}}}, \tag{3.7}$$

where OD_{sat} has to be determined as the highest optical density measurable. For a reasonable determination, one waits until the atom cloud expands (typically a few ms) so the centre can be considered to have evenly distributed atoms. Since possible errors between the measured and modified optical density increase with bigger differences between them, it is advised to image the MOT-cloud after a certain time of free expansion until OD_{meas} is of the order of OD_{sat}. The second error arises from intense laser light, which affects the population of the atoms drastically. For high laser intensities of the order of I_{sat} the absorption cross-section reads

$$\tilde{\sigma} = \sigma\frac{1}{1 + I/I_{\mathrm{sat}}}, \tag{3.8}$$

which yields

$$OD_{\mathrm{actual}} = OD_{\mathrm{mod}} + (1 - e^{-OD_{\mathrm{mod}}})\frac{I_0}{I_{\mathrm{sat}}} \ . \tag{3.9}$$

To keep the correction value as low as possible the intensity of the imaging beam is chosen to be $I_0 \approx 0.1 \times I_{\mathrm{sat}}$.

To calculate the overall number of atoms in the atomic cloud we have to integrate the measured and compensated optical density $OD = n\sigma(\omega)$ over the whole cross-section of the cloud.

$$N_{\mathrm{total}} = \int_{-\infty}^{+\infty}\int_{-\infty}^{+\infty} n(x,y)\mathrm{d}x\mathrm{d}y = \frac{1}{\sigma}\int_{-\infty}^{+\infty}\int_{-\infty}^{+\infty} OD_{\mathrm{actual}}\mathrm{d}x\mathrm{d}y \tag{3.10}$$

Note that $n = n(x,y)$ is the number of atoms along the axis of propagation of the imaging light, which is why it is also referred to as the atom column density, where a pixel of the acquired image corresponds to a column of atoms.

3.1.2 Time of flight measurement

The next parameter we want to determine is the temperature of the atoms in the atomic cloud achieved in the magneto optical trap (MOT) and optical molasses. Therefore the cooling mechanism is switched off after a trapping cycle and the atom cloud expands according to its velocity distribution. Looking at the expanding cloud during several time steps directly allows to determine the temperature. The temperature of an ideal gas is given by

$$\frac{M}{2}\overline{v^2} = \frac{3}{2}k_B T, \tag{3.11}$$

where M is the mass of the atom, $\overline{v^2}$ the atoms mean quadratic velocity and k_B is the Boltzmann constant. Modelling the atomic vapour as ideal gas is a good approximation, since the interaction between the atoms is much lower than the mean kinetic energy of the atoms. The velocity distribution of an ideal gas is the Boltzmann distribution which reads for one velocity component as

$$f(v)\mathrm{d}v = \sqrt{\frac{M}{2\pi k_B T}} \exp\left(-\frac{Mv^2}{2k_B T}\right) \mathrm{d}v \ . \tag{3.12}$$

Note that only the distribution in one direction is necessary since we are looking at the expansion in all directions independently. The velocity distribution corresponds to a Gaussian distribution for the velocity, which when compared to

$$f(x)\mathrm{d}x = \frac{1}{\sqrt{2\pi}\sigma} \exp\left(-\frac{x^2}{2\sigma^2}\right) \mathrm{d}x \tag{3.13}$$

allows to obtain the standard deviation in velocities as

$$\sigma = \sqrt{\frac{k_B T}{M}} \ . \tag{3.14}$$

When a cooled gas with a certain temperature can freely expand, the expansion Δ increases approximately according to

$$\Delta = \sqrt{\frac{k_B T}{M}}\ t, \tag{3.15}$$

which gives a final size at a given temperature T of

$$L_{\mathrm{cloud}} = L_{\mathrm{initial}} + \Delta = L_{\mathrm{initial}} + \sqrt{\frac{k_B T}{M}}\ t \ . \tag{3.16}$$

Note that this approximation is only valid for low temperatures, short times and no thermal interaction with the environment.

To actually measure the size of the atom cloud, absorption imaging as described above is performed. The image of the compensated optical density OD_{actual} is taken to fit a Gaussian distribution across 2 perpendicular lines through the centre of the cloud. Note that the Gaussian is fitted not due to the Boltzmann distribution introduced before, which is a distribution of velocities, but because of the expected spatial distribution of the atoms in the MOT-cloud. We define the border of the atomic cloud as the values where the density distribution drops to $1/e^2$. Note that lengths are measured by counting pixels according to

$$l = \frac{n_p s_p}{\beta}, \tag{3.17}$$

where n_p is the number of pixels, s_p the size of a pixel and β the magnification of the imaging setup. Since resonant light is absorbed by the atoms in the cloud, the kinetic energy is altered and the temperature increases. Therefore, the time of flight measurement to determine the temperature is performed sequentially, where the time between releasing the atoms from the MOT and imaging the cloud is increased from shot to shot. Ultimately the temperature can be determined from the size of the atom cloud via

$$T = \frac{M}{k_B t^2}(\frac{s_p}{\beta})^2(n_t - n_0)^2, \tag{3.18}$$

where n_0 and n_t stand for the length of the cloud measured in numbers of pixels on the CMOS chip acquired initially and after waiting for the time t, respectively.

3.2 Design of the Imaging setup

In absorption imaging one wants to take images of a shadow cast by an atomic cloud. Since a shadow cannot be imaged in the same sense a normal object (e.g. in photography) would be imaged, it is necessary to image both the shadow of the atomic cloud and the incident beam at the same time. The absorption imaging system has to be able to evenly illuminate the camera with a collimated laser beam coming from far behind the atom cloud and focus an image from the atomic cloud on the camera. This can be done by a two-lens system that acts as a telescope for the imaging light and as a microscope for the atomic cloud.

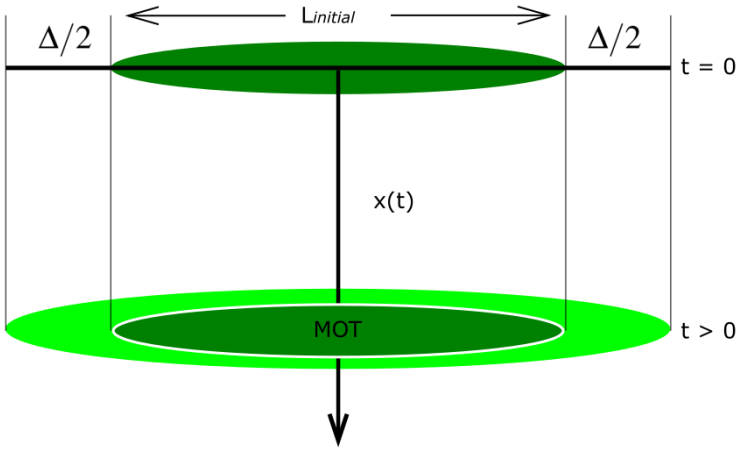


Fig. 3.1 When the lasers that trap the MOT-cloud (dark green) are switched off, the cloud begins to fall, since the velocities of the atoms are small and the earth's gravitational pull accelerates the atoms. At the same time due to the finite temperature of the atoms the MOT-cloud expands. The expansion over time directly allows for determination of the temperature.

3.2.1 Optical scheme

Two-lens systems are a very basic concept in optical applications, where for thin lenses the lens formula reads

$$\frac{f'}{a'} + \frac{\bar{f}}{a} = 1. \tag{3.19}$$

Here f' is the focal length on the imaging side, $\bar{f}$ is the focal length on the object side and a' and a are the distances of image and object to the principal planes of the lenses, respectively. For a two-lens system as sketched in Fig. 3.2 one can derive the focal length of the combined system to be

$$f' = \frac{f_1' f_2'}{f_1' + f_2' - e}, \tag{3.20}$$

where e is the distance between the lenses. In a typical telescope configuration (here a Kepler-telescope) two positive lenses are placed in a distance $e = f_1' + f_2$, so the combined focal length f' becomes infinite. This way a collimated beam entering the system on the one side is imaged at infinite distances, which means it is collimated. The change in diameter of the beam can be determined via the magnification β, which

becomes for infinite object distance (collimated beam)

$$\beta = -\frac{f_2'}{f_1'} \ . \tag{3.21}$$

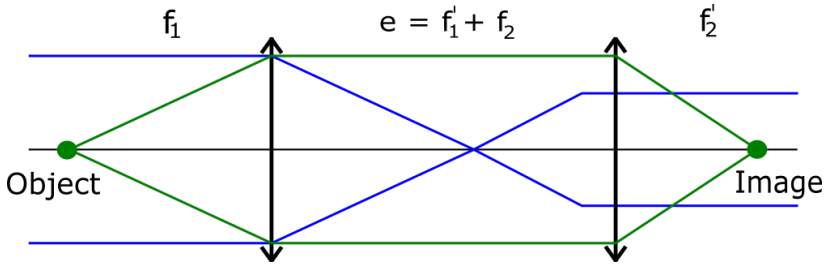


Fig. 3.2 Scheme of a Kepler-telescope consisting in 2 positive lenses. The telescope configuration will transfer a collimated beam into a collimanetd beam with different beam diameter and an object placed at the distance f_1 will be imaged into the focal spot at a distance f_2'. The lenses in an afocal telescope are placed $e = f_1' + f_2$ apart from each other.

At the same time we can use this system to image an object in finite distances. The most convenient case is when the object is placed exactly in the focal spot of the first lens. Objects in the focal spot of a lens will be imaged at infinite distances and vice versa. That way the first lens is not producing an image but is collimating the light from the object and the second lens will focus it in its focal spot, where the same results for the magnification β are valid. This two-lens imaging system is the perfect candidate for our purpose. A collimated laser beam will stay collimated and illuminate the camera, while the atomic cloud placed at the focal spot of the first lens will be imaged on the camera, which has to be placed in the focal spot of the second lens. To calculate the possible minimum in resolution, one has to determine the numerical aperture

$$NA = n \sin(\alpha), \tag{3.22}$$

where n is the refractive index of the medium between the object and the first lens (usually $n = 1$) and 2α is the maximal angle of the cone of light that can enter the lens. The diffraction limited resolution for a given wavelength λ can be determined by

$$d_{\min} = 0.61 \frac{\lambda}{NA} \ . \tag{3.23}$$

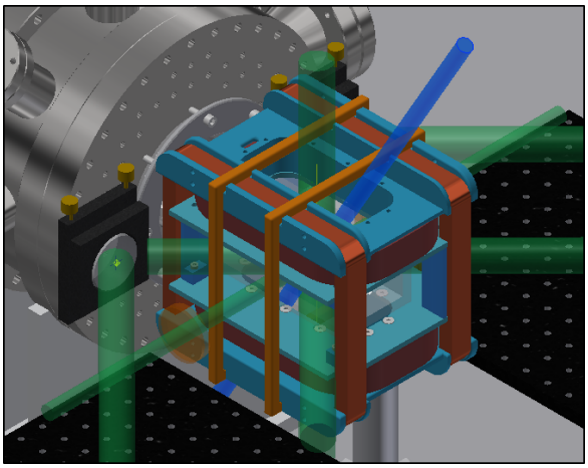


Fig. 3.3 A cage holding 3 pairs of magnetic coils (MOT-, bias- and compensation field, respectively) is put around the glass cell. This design, allows for great overall optical access to the nanofiber and the MOT-cloud. The huge green plotted lasers represent the cooling and trapping lasers, which enter the chamber diagonally in the horizontal plane and straight from top and bottom in the vertical direction. The small green beam coming from the left shows the horizontal imaging beam, which can pass the cell unhindered. The blue beam is a planned laser for a proposed experiment of creating a bragg-grating in the fiber, which is why imaging along this axis is therefore not possible. For the vertical imaging, no separate axis for optical access is available and the vertical MOT-laser setup will be used for that.

3.2.2 Horizontal setup

As one can see in Fig. 3.3, the horizontal setup has a direct line of sight through the glass cell. Therefore the horizontal axis was primarily chosen as the imaging axis where due to only a few minor space constraints the setup can be carefully designed to get good imaging results. A similar setup as proposed in Smith et al. (2011) was used as design basis. In Fig. 3.4 a typical setup of absorption imaging is shown. As one can see, the beam illuminating the atom cloud has to have a diameter bigger than the cloud, to have a suitable intensity across the whole region where the beam intersects the atomic cloud. The MOT itself is designed to form a strongly elongated cigar shaped atom cloud with 1 mm in diameter and 10 mm along the elongated axis. The absorption imaging should work on the resonant Cesium D2 transition at 852 nm.

Constraints and benchmarks

To properly design the imaging setup one has to consider several physical and optical constraints. The first constraint is the need for an appropriate cross-section of the

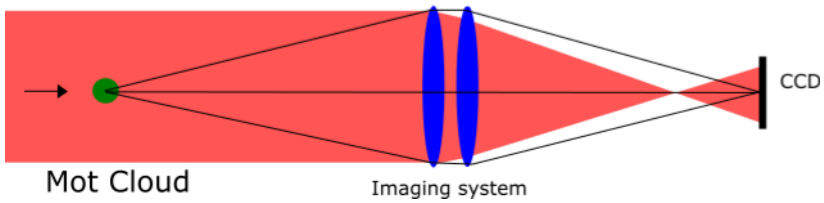


Fig. 3.4 The MOT-cloud which is placed at the focal spot of the first lens will be imaged into the focal spot of the second lens, where the camera is placed. The imaging beam coming collimated from the left side, illuminates the whole cloud and gets attenuated accordingly. Since the two lenses are quite close to each other, the imaging beam is not collimated on the right side, but still big enough to illuminate the camera and allow for a good contrast to see the shadow cast by the MOT-cloud.

imaging beam. To image a beam of a size well bigger then the MOT's lateral extension of 1 cm, it was decided to limit the system on the biggest standardized available lenses with a diameter of 2 inch ($\approx$ 50.8 mm). These lenses are available with suitable anti-reflection coating for a wavelength of 852 nm and come with a lot of standardized 2 inch optical accessories, which makes alignment and mounting convenient.

A well known systematic error in optics is the so called spherical aberration. Beams entering spherical lenses above a certain distance from the optical axis are refracted stronger than beams in close vicinity of the optical axis (paraxial approximation). Since this would affect the imaging quality drastically for 2 inch lenses, achromatic lenses are used. An achromatic lens is a doublet of lenses with different refractive indices to correct for wavelength dependent spherical aberrations. To keep the setup as compact as possible and have the image quality unaffected by the exact alignment of the lenses with respect to each other, it was decided to put them exactly after each other, connected via a suitable mount. This will not perturb the imaging, since an object placed in the focus of the first lens is imaged into the focus of the second lens independent of the distance between them. The imaging beam on the other hand, will be focussed, but since the focal length of the connected system is smaller than the focal length of the second lens (where the camera is placed) the imaging beam arrives divergent and spread big enough to illuminate the CMOS chip (Fig. 3.4). This can be done, although not the whole chip will be illuminated like that, since the analysis will anyway just look at a region of interest, where the picture taken with the illuminating beam will sufficiently be subtracted from the final image (see section 3.1.1). The imaging setup is placed on a breadboard of 40 cm width mounted about 30 cm above the laser table to be perfectly aligned with the glass cell. Since the laser setup for the

MOT beams is also placed there, the imaging setup should not take up to much space in total.

The last constraint which has to be taken into consideration is the expected temperature of the MOT cloud. When the trap is switched off, the cloud will freely fall due to gravity and expand at the same time. An estimation is necessary to find the right size of the camera chip and magnification of the setup. To do so, one uses Eq. (3.16) to calculate the expansion of the cloud and

$$x(t) = g\frac{t^2}{2} \tag{3.24}$$

gives the distance the cloud falls in the earth's gravitational field. The mass of Cesium atoms is $m = 132.3\text{u}$, where $\text{u} = 1.66 \times 10^{-23}\,\text{kg}$, and $k_B = 1.38 \times 10^{-23}\,\text{J/K}$ is the Boltzmann constant. In a worst case estimation, $T = T_D = 125\,\mu\text{K}$ was used, so for a time of flight of 30 ms the cloud would fall 4.4 mm and expand by 2.7 mm.

Within this constraints several combinations of lenses were simulated using a ray-tracing programme and finally, a combination of lenses with focal lengths of 300 mm and 150 mm was chosen. The theoretical magnification of this system is $\beta = 1/2$ with a calculated resolution of 6.16 µm. The camera[1] used to image the MOT-cloud has a sensor size of 1/1.8 inch (7.2 mm × 5.35 mm) with a pixel size of 5.3 µm × 5.3 µm, which is slightly above the theoretical resolution. Additionally the CMOS chip has an enhanced infrared spectral sensitivity.

Simulation

A ray-tracing simulation[2] for several combinations of lenses was performed to decide on an optimal setup. Additionally, once the lenses are chosen, the numerical simulation allows for optimization and characterisation of the setup. For the horizontal image system the combination of a 300 mm and a 150 mm focal length achromat showed to have the best simulation outcome.

To find the perfect placement of the lenses, paraxial ray optimisation was performed. To do so the first lens was simulated to collimate a beam coming from the object to find the ideal distance between object and lens. After that the second lens was added and an autofocus optimisation could be performed to find the perfect place for the camera.

[1] Matrix Vision mvBlueFOX3-1013GE
[2] OSLO Trace Pro

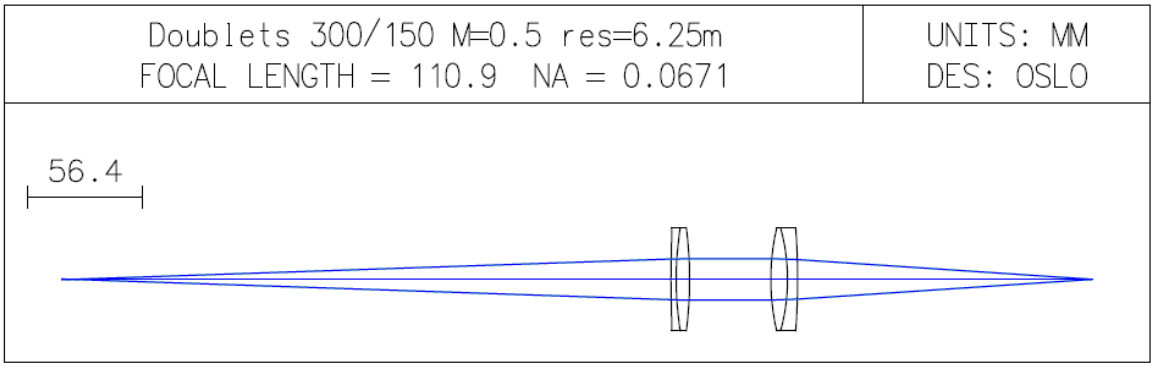


Fig. 3.5 Ray tracing result of the horizontal imaging setup. Scattered light from the MOT (focal spot on the left) is collimated after the first lens. Placing the lenses in the right distance apart from each other is therefore not important for the quality of the image.

The next step in optimisation is calculating the point spread function at the focus of the setup, where many beams are individually traced through the system. This way it is possible to determine whether the setup is diffraction limited or flawed by aberrations. Since we are using achromatic lenses the system is indeed diffraction limited, which is a satisfactory quality attribute of the system. Simulation to determine the resolution can be done by calculating the modulation transfer function MTF. This method compares the contrast of an object to the contrast of its image. The object consists in a mathematical grating with decaying spatial frequency and the envelope of the modulated grating on the imaging side, plotted versus the spatial frequency (distance of a pair of next neighbour lines in the grating) is a direct measure of the quality of the imaging system. The first zero crossing, which is the cut-off frequency, is indirectly proportional to the resolution of the system $d_{\mathrm{min}} = 1/f_{\mathrm{cutoff}}$. For this setup the simulated resolution is 6.25 µm.

The MTF was also used to characterise the stability of the system in terms of misalignment of the object-lens and lens-camera distance. The resolution remains unchanged for a misalignment of the object of ± 1 mm and a misalignment of ±0.3 mm of the camera. Although this values seem to be very low, it is possible to get a very good MTF for a misaligned object by correcting the distance between the camera and the lens-system accordingly. The simulation results for the imaging setup are summed up in Table 3.1.

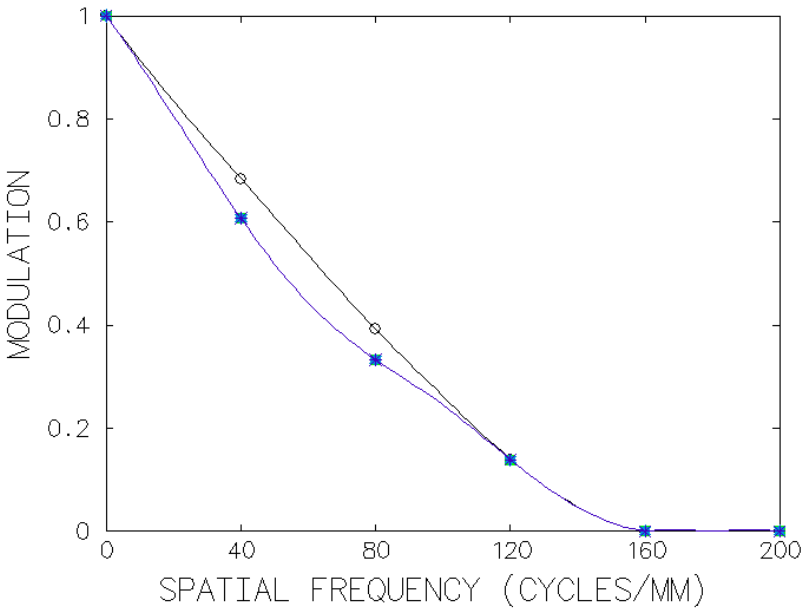


Fig. 3.6 Modulation transfer function (MTF) for the horizontal imaging setup. The ideal envelope of the modulation is plotted black, while the simulated MTF is plotted blue. The resolution minima is indirectly proportional to the cut-off frequency of the MTF, which is about 160 cycles/mm.

Imaging beam

To create an imaging beam that has an appropriate diameter to illuminate the whole atom cloud, an optical setup to collimate and widen the beam to the desired diameter is needed. In a first step a special fiber mounted telescope is used[3], which creates a collimated beam with a theoretical output diameter of 7.8 mm. In a second step the beam gets further enlarged with a telescope of magnification $\beta = 3.3$ to finally arrive at a beam diameter of 25.7 mm, which is suitable to evenly illuminate our MOT with expected biggest expansion of about 10 mm.

To have a compact and perfectly aligned setup, all mentioned lenses were mounted in a cage system. Additionally a small glass plate was put between the fiber coupler and the telescope to reflect about 4% of the beam onto a photo-diode. Since both are also part of the cage system, crucial alignment only has to be done once, after that the rack can be considered to be one optical device which simplifies further alignment of the overall setup. The intensity of the beam arriving at the place of the MOT-cloud was carefully measured to calibrate the photo-diode. The output signal of the diode is connected to an intensity stabilization device, which is controlled via the overall

[3]Thorlabs Air-Spaced Doublet Collimator F810APC-842, NA = 0.25, f = 36.18 mm

Table 3.1 Theoretical and simulated parameters of the horizontal imaging setup

	theoretical	simulated
lens 1 [mm]	300	294
lens 2 [mm]	150	145
resolution [μm]	6.16	6.25
NA	0.08	0.067
β	0.5	0.5

experimental control software. Therefore a stable and well known intensity of the imaging beam can be guaranteed.

Experimental setup

The experimental setup for the horizontal imaging setup is shown in Fig. 3.7. The imaging beam of resonant light $\lambda = 852\,\text{nm}$ is taken from the same laser as the cooling light for the MOT and coupled into the collimation and beam widening setup, shown on the left side of the scheme. Two 2 inch mirrors are used to align the laser vertical and horizontally. After going through the glass cell and passing the atom-cloud, the beam is imaged onto the camera via a second mirror. The mirror is used to fold the beam-line, since there is not enough lateral space on the breadboard and additionally allows to move the image across the CMOS chip as needed. The camera itself is placed on a translation stage that allows for fine adjustment of the distance between the lenses and the camera on a micrometer scale. The glass cell is anti-reflection coated on the

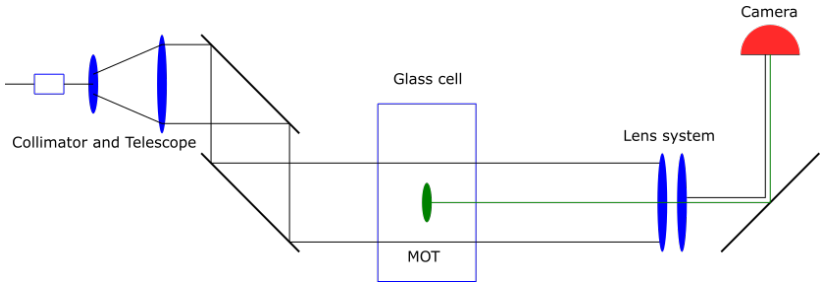


Fig. 3.7 Scheme of the horizontal imagaing setup. The imaging light (black) is coupled in, collimated and widened in the first telescope setup. After passing the glass cell and being absorbed by the atom-cloud, the imaging beam is directed to the camera to illuminate the CMOS chip. The shadow cast from absorption is displayed in green.

outside to get as much light into the cell as possible. Unfortunately coating the cell on the inside is technically not possible so passing laser beams might create standing waves

in the cell and form interference patters on the camera. Fortunately such patterns have yet not been observed. For a good measurement outcome the imaging beam should have an intensity of $I \approx 0.1 I_{\text{sat}}$ with the saturation intensity for linear polarized light for Cesium of $I_{\text{sat}} = 1.66\,\text{mW/cm}^2$, which results for the horizontal beam diameter of about 25 mm in a beam intensity of 0.82 mW.

Measuring the scaling of the imaging setup by imaging a ruler revealed that the field of view is 12.5 mm × 10 mm, where a pixel corresponds to 9.8 µm which resulting in a magnification of $\beta = 0.54$. This value is slightly bigger than the simulated resolving power and suits our needs perfectly. Note that for a good imaging quality it is advised to have pixel sizes of the order of the resolution, otherwise you lose information (pixel size too big) or create a possibility of recording image artefacts and being prone to more noise (pixel too small).

3.2.3 Vertical setup

Usually, for a time of flight measurement of the atom cloud to define its temperature, imaging the MOT from one direction is sufficient. Adding a second perpendicular line of sight towards the glass cell for imaging was decided primarily because it is necessary for the polarization adjustment in the nanofiber (see Chapter 4). Nevertheless a second direction for absorption imaging comes with several advantages, like smaller errors in temperature measurement. One issue that occurs is the atom cloud leaving the exact focus of the imaging setup due to the cloud falling down in the gravitational field of the earth. What is seen is a movement across the CMOS chip in the horizontal camera and falling out of focus in the vertical camera. Therefore combining both acquired data enables better error correction.

Additionally a second direction allows to check whether the MOT cloud has the desired shape. Note that imaging only presents a projection of the cross-section of the cloud in one plane. As example given, a slightly s-shaped cloud in one plane would still look cigar-shaped when projected to the perpendicular plane. Imaging from two directions eliminates uncertainties regarding this problem. Finally the second imaging axis is necessary for the alignment of the nanofiber with respect to the atom-cloud for the same reasons stated above.

Constraints and benchmarks

As one can see in Fig. 3.3 the line of sight for a vertical imaging setup is blocked by the laser cooling setup and a slightly tilted line of view is not possible due to spatial

constraints. It was decided on using the setup for guiding the MOT-beams to the glass cell as part of the imaging system. To do so, the imaging beam needs to be inserted and ejected at two suitable points without interfering with the beam-line of the host setup. Since the imaging setup is used after the MOT beams are shut off, there will be no interferences. Besides that, no spacial constraints are present since on the optical table and on the breadboard above the glass cell plenty of space is available to place optical components. Unfortunately using a setup like in the horizontal plane cannot be done since the beam is passing the MOT setup, which makes it impossible to place the MOT-cloud in the focus of the first lens. Additionally the imaging beam will pass two telescopes used to widen and narrow the lasers for MOT cooling, which means that the shadow cast from the atomic-cloud passes a narrowing telescope, which has to be considered in the imaging setup. The used Galilei-telescopes in the MOT setup are in an afocal configuration, which images collimated beams as collimated beams. An object in finite distances to the first lens ($a \approx f$) will be virtually imaged in front of the second lens, or in other words, a beam from the MOT-cloud would strongly diverge after the telescope. Therefore, it was decided to take 2 inch lenses, placed as close as possible to the narrowing telescope to catch as much of the divergent light as possible. For easy to handle data-acquisition and analysis the second imaging setup should contain the same camera model as the horizontal setup, which constraints the final size of the image to an 1/1.8 inch sensor and limits the necessary resolution to about 5.3 µm. The final decision for lens types and placement again could only be made after simulation and ray tracing.

Simulation

For reasonable ray tracing, the imaging setup as well as the narrowing telescope have to be simulated. The exact distance between the MOT cloud and the first lens cannot be determined, but approximated from AUTO-CAD[4] drawings of the experiment to be about 50 cm. A combined system of a 150 mm plano-convex lens and an achromatic lens with a focal length of 250 mm were used. Again paraxial ray optimisation was used to find the perfect position of the first lens, to collimate the imaged beams. Therefore the second lens can also be directly placed after the first lens to keep the system as compact as possible and easy to align. The imaging beam which enters the setup collimated will be focussed but reaches the camera spread enough to illuminate the CMOS chip sufficiently to have a suitable background.

[4] 3D computer-aided design (CAD) and drafting software

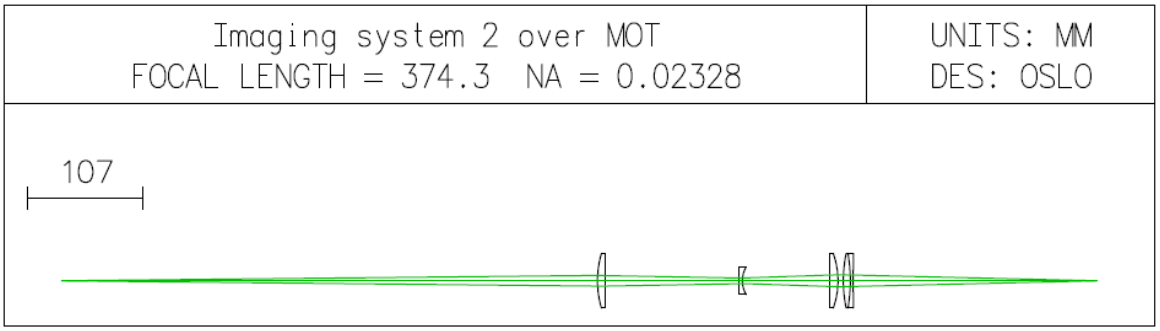


Fig. 3.8 Ray tracing result of the vertical imaging setup. The first two lenses simulate the widening telescope for the MOT-lasers which would go through the setup from right to left. The second two lenses simulate the imaging setup, which needs to compensate for the divergence of the beam after the telescope. The imaging beam goes from the left to the right.

The resolution of the setup was calculated from the numerical aperture of the first lens to be 0.05 but simulation with optimized values and consideration of aberrations gives $NA = 0.023$ which would result in a slightly lower resolving power. Analysis of the modulation transfer function yields an ideal resolution of about 10.4 µm. Further analysis showed, that for an increasing distance of the object due to falling during the TOF measurement, the MTF fits the function of an ideal system close to the cut-off frequency even better, while the overall performance stays the same. Therefore a mismatch in focal length of the object-lens distance would not affect the quality of imaging drastically and probable errors introduced in the horizontal imaging can be compensated. Nevertheless, it was not possible to design a two lens system which is uniquely diffraction limited, without using an entrance pupil. The simulation outcome of the most important properties can be found in Table (3.2).

Table 3.2 Theoretical and simulated parameters of the vertical imaging setup

	theoretical	simulated
lens 1 [mm]	125	-
lens 2 [mm]	250	227
resolution [μm]	10.2	10.4
NA	0.05	0.023
β	0.6	0.43

Experimental setup

As on can see in the sketched experimental setup plotted in Fig. 3.9 the imaging beam is inserted into the MOT laser setup via a polarizing beam splitter (PBS) cube. The cube is combined with two $\lambda/2$ waveplates and placed in a way, that the cooling laser can pass the PBS unhindered and the imaging beam is reflected into the setup. For alignment two mirrors are placed before the PBS, and the laser which is withdrawn from the same source as the horizontal imaging light, is coupled in and collimated with a small aspheric lens system at the beginning of the setup. On the other side, after the beam has passed the glass cell and the narrowing telescope, a PBS and the lens system is put as close to the telescope as possible. This effectively allows to catch as much light coming from the glass cell as possible. At the same time light that is diverging a lot from the telescope will not pass the PBS since it is only of one inch size and therefore acts as an aperture for the imaging setup. This has an positive effect on the quality of the image, since light outside the paraxial area is not entering the imaging setup and aberrations introduced by the lenses can be decreased. Measuring the scaling of the imaging setup revealed a field of view of 1.9 mm × 1.5 mm, where a pixel corresponds to 14.8 µm, which is again slightly above the simulated resolution minima and therefore perfectly suitable for our needs. The resulting measured magnification of the system is $\beta = 0.36$. The camera is mounted on a translation stage to enable focussing, and a mirror is added after the imaging setup to move the image across the CMOS chip.

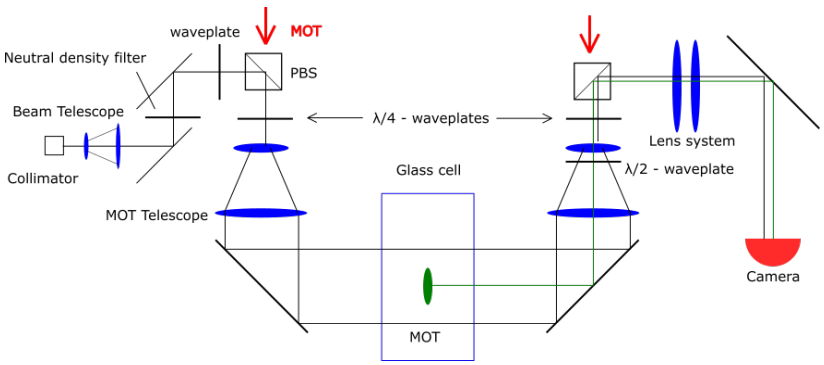


Fig. 3.9 Scheme of the vertical imagaing setup. The imaging light (black) is inserted into the MOT setup via a PBS and widened in the first telescope. The widened imaging beam passes the glass cell, gets attenuated by the atom-cloud and passes a second telescope. After that, the beam is withdrawn from the MOT setup with a second PBS and imaged onto a CMOS chip. The shadow cast from absorbing the imaging beam is displayed in green.

Another issue arising from passing the MOT setup is, that the imaging beam will have a circular polarization while passing the MOT-cloud. This is due to the fact that the MOT needs to be operated with circular polarized light. Since the polarizing beam splitter used to insert the imagining beam transmits light of a specified linear polarization and reflects light of the perpendicular linear polarization the $\lambda/4$ waveplate needs to be put after the PBS to change the polarization of the MOT-beam. Therefore the polarization of the vertical imaging beam is also circular. This needs to be considered when adjusting the intensity for absorption imaging, since the saturation intensity of circular polarized light ($I_{\mathrm{sat}} = 1.1\,\mathrm{mW/cm^2}$) is different from the saturation density of linear polarized light. The beam diameter after the fiber coupling and collimation is 1.3 mm. A small 1/2 inch diameter telescope magnifies the beam by a factor of 4 and the MOT-telescope widens the beam by another factor of 3. Therefore the final beam has a diameter of 15.6 mm, which is suitable for illuminating the MOT-cloud. For this beam configuration the necessary intensity is 0.21 mW, which is about a factor of 4 smaller than in the horizontal setup. Since the beam for the vertical and the horizontal imaging arms are taken from the same laser, only one intensity stabilization feedback loop is used. To ensure the right intensity to arrive at the MOT-cloud, the beam in the vertical setup needs to be attenuated by a factor of 4 by a neutral density filter.

3.2.4 Summary of experimental parameters

In Table 3.3 a complete overview and comparison of all experimental parameters of the two imaging setups is given. Note that the values correspond to the measured and simulated experiments. The numbers stated for lens types are Thorlabs item numbers, so one can look up details of the specifications on their website.

3.3 Summary and Outlook

Sufficient pre-cooling and trapping of atoms is a prerequisite to successfully load a nanofiber-based dipole trap. For optimization of the cooling and trapping mechanism, an imaging setup to determine the atom-clouds shape and temperature was desired. It was shown, by taking into consideration the physical and optical constraints, given by the experiment, how an imaging design for absorption imaging was theoretically planned and simulated. Experimentally, the imaging setup could be implemented successfully

Table 3.3 Comparison of simulated and measured parameters of the imaging setups

	horizontal	vertical
1st lens	AC508-300-B-ML	LA1417-B
2nd lens	AC508-150-B-ML	AC508-250-B-ML
camera	mvBlueFOX3-1013GE	mvBlueFOX3-1013GE
object-1st lense [mm]	294	-
last lens - camera [mm]	145	227
field of view [mm]	12.5×10	18.9×15.1
size per pixel [μm]	9.8	14.8
resolution [μm]	6.16/6.25	10.2/10.4
NA	0.08/0.067	0.05/0.023
β	0.5/0.53	0.43/0.36

and the experimental parameters of the imaging system are in good accordance with the previous simulation.

The imaging setup built in the course of this thesis could already be used to image the atom cloud, allowing for optimization of the beam intensity balance and position of the cloud with respect to the beam intersection area and magnetic field gradient centre. By doing so, a stable MOT-cloud was established and first preliminary measurements were taken. Probing the atom cloud can be done right after loading the MOT, by switching off all light fields and the magnetic quadrupole field before taking absorption images. Alternatively, the light fields can remain on after switching off the magnetic fields, to further cool the atoms in an optical molasses and then switch everything off to probe the atomic cloud. In Fig. 3.10 one sees a sequence of absorption images for a time of flight measurement, taken after loading the MOT for one second and subsequent cooling in an optical molasses for 5 ms. The temperature could be estimated to be approximately 50 µK (see Fig. 3.11a) with an approximate peak optical density of 2.2. As one can see, the cloud expands into vertical and horizontal directions with different speeds, which is an indicator for a not yet perfectly aligned cooling setup, e.g. unbalanced power in the MOT lasers or uncompensated earth's magnetic fields. Additionally on can see the fall of the atomic cloud due to earth's gravity, as shown in Fig. 3.11b.

For the acquisition of experimental results, a specialized programme to interface the cameras and analyse the recorded data was written. The programme allows for a live view from the cameras, direct access to the camera settings, several real time measurement routines (e.g. rulers, intensity plots or region of interest control) and

control over the time of flight measurement parameters. Details of the code and a manual for the graphical user interface are given in the Appendix.

In the next steps of setting up the overall experiment, the absorption imaging setup will be of high importance, to further optimize the MOT setup. The aim is to have faster loading times, higher atom numbers in the cloud, bigger size of the cloud and lower temperatures. Finally, the efficiency for loading atoms into the nanofiber based dipole trap via an optical molasses should be as high as possible, yielding a good basis for subsequent experiments, such as the implementation of an quantum memory.

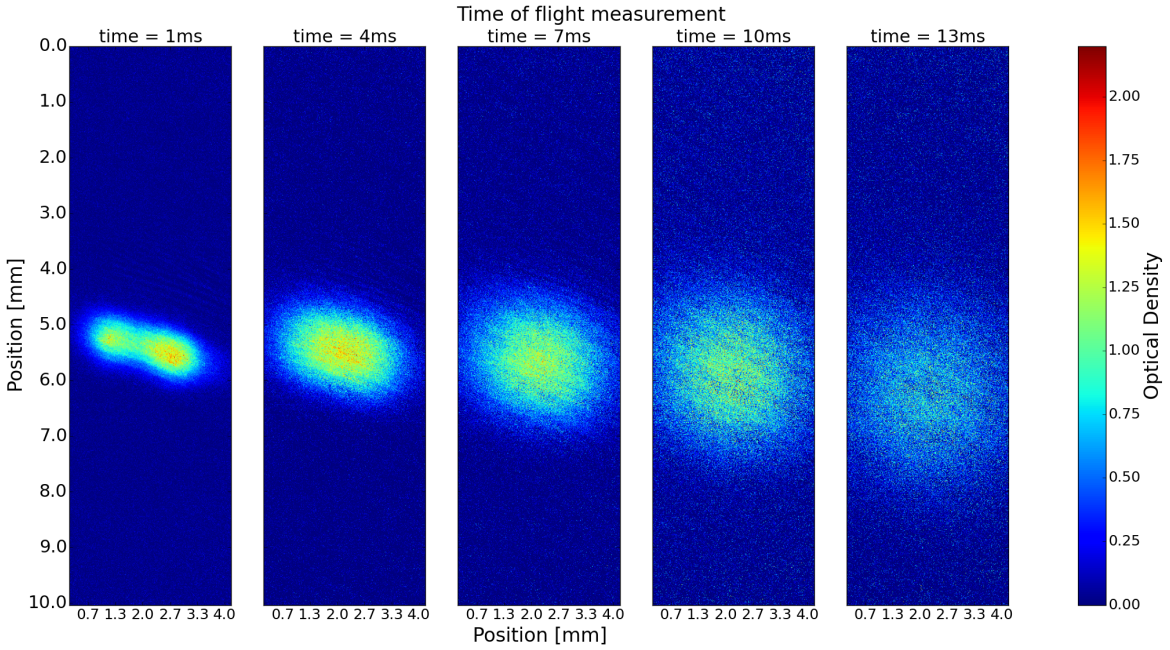
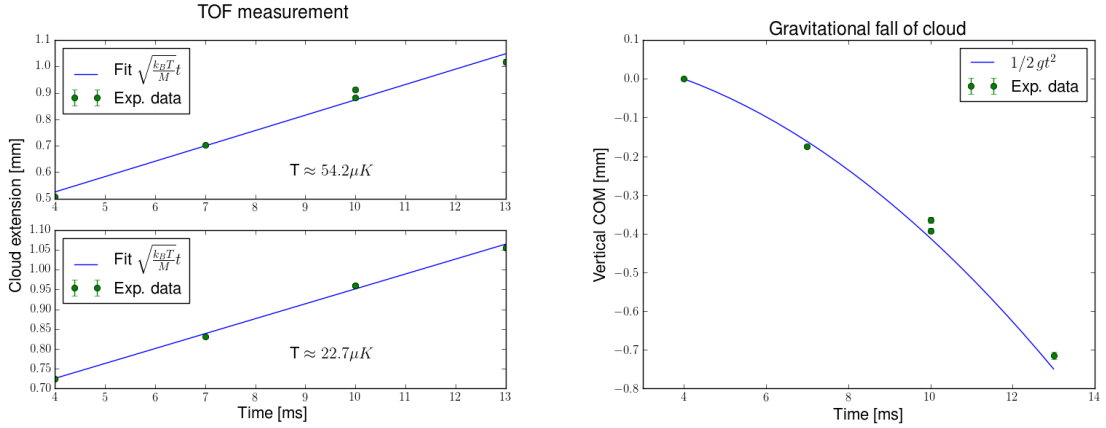


Fig. 3.10 Time of flight measurement of the atomic cloud after being cooled in a MOT and subsequent optical molasses for 5 ms. As one can clearly see, the cloud expands due to the finite temperature of the atoms and falls down due to gravity. The highest measured optical density is about 1.5 for a cloud of approximately 3.2 mm × 0.8 mm size. The temperature could be estimated to be 50 µK.



(a) (b)

Fig. 3.11 a) Fit to the size of the cloud versus time, after the cooling has been switched off, to determine the temperature via the slope of the fit. As one can see, the cloud expands unevenly in horizontal and vertical direction, which corresponds to different temperatures. A conservative estimation yields a temperature of approximately 50 µK. b) Plot of the position of the centre of the atom cloud, determined via Gaussian fits of the shape. As one can clearly see the cloud's temperature is sufficiently low to see the atoms mutually falling in the gravitational pull of the earth.

Chapter 4

Polarization Imaging

After having discussed cooling and trapping of Cesium atoms close to the nanofiber, as prerequisite for loading the nanofiber-based dipole trap, one has to make sure that the desired trapping configuration is realized. As described in section (1.2.3), trapping atoms on two sides along the fiber critically depends on the orientation of polarization of a quasilinearly polarized guided field in the nanofiber. Additionally, for an ideal nanofiber trap, the trapping configuration should remain unchanged over the whole waist, which cannot be guaranteed beforehand.

In this chapter, I will introduce a technique to determine the local polarization in the waist of the fiber, which can be inferred from scattered light of the nanofiber, and discuss the experimental implementation of the imaging setup.

4.1 Polarization in the nanofiber

In an experiment containing optical glass fibers, where the polarization of the guided light is important, typically polarization maintaining fibers are used. These fibers usually consist of two boron rods on opposite sides of the core of the fibers. Those rods introduce mechanical stress on the core during the process of manufacturing and therefore create birefringence in a way, that light linearly polarized along this axis maintains its polarization over very long distances. Unfortunately it is not possible to produce nanofibers from polarization maintaining fibers in the fiber-pulling rig, since the boron starts boiling at hydrogen oxygen flame temperatures. The boiling boron diffuses into the cladding of the fiber, and the nanofiber gets completely opaque. Using a standard optical glass fiber instead does not guarantee a stable polarization due to environmental influences. Bending and twisting the fiber as well as temperature fluctuations change the birefringence of the fiber. The fiber needs to be fixed rigorously

on the optical table and be thermally stabilized so the changes of birefringence are minimized. Usually one cares solely about the polarization at the output of a fiber, which can be measured with a suitable polarimeter and adjusted either via a set of waveplates before coupling the laser into the fiber or via the use of paddle polarization controllers, where the fiber gets bent and twisted in a controlled way.

In the case of a nanofiber trap, we want to know the polarization exactly at the position where the atoms should be trapped in a later stage. This information is not directly accessible and a knowledge of the polarization before or after the fiber has, without further investigation, no direct correlation to the polarization in the nanofiber. One can realize a measurement of the local polarization in the nanofiber by analysing light scattered out of the fiber. Every nanofiber contains a few speckles of surface imperfections and inhomogeneities in the bulk silica (see Fig. 4.1), which scatter a small amount of the fiber guided light. It is assumed that these dipoles are point-like due to their small extensions and conserve the local polarization of the light in the fiber. This assumptions allow for indirect determination of the polarization of the guided light by investigation of the dipole emission pattern.

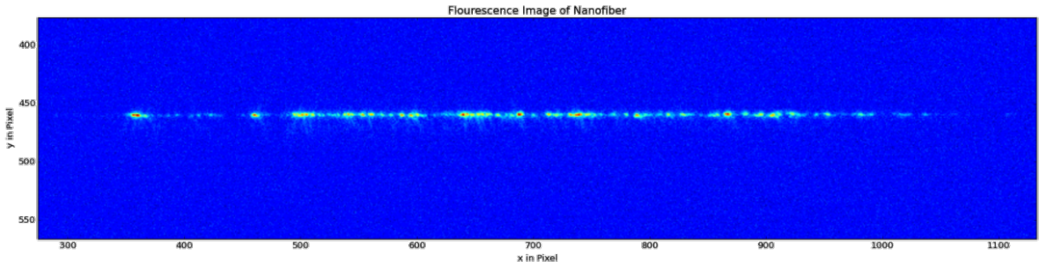
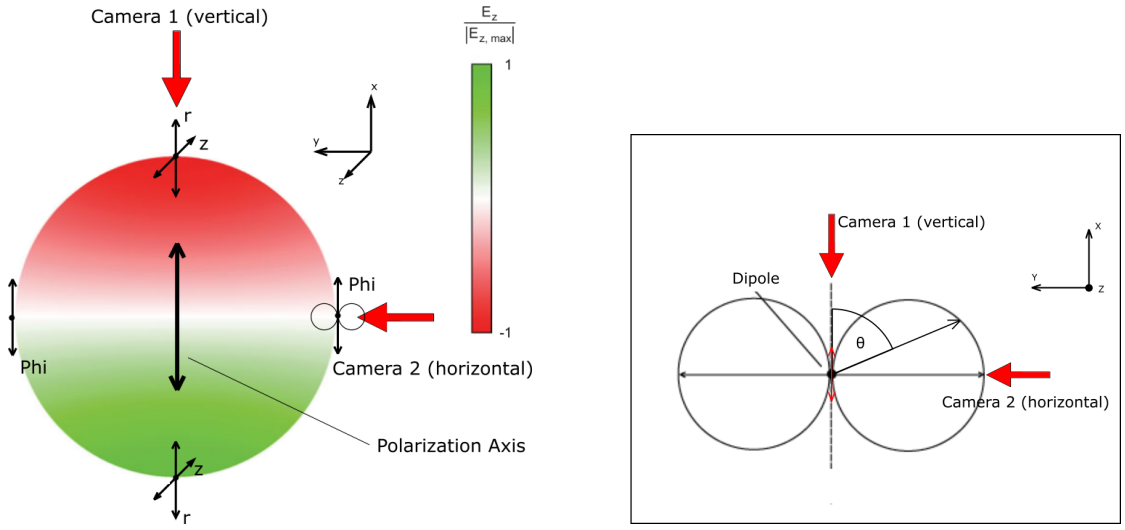


Fig. 4.1 Scatterers on a nanofiber, such as surface imperfections or inhomogeneities in the bulk silica, appear as fluorescing spots on an image.

The intensities measured by the cameras can be considered to be the sum of the light fields scattered by single emitters on the fiber surface. A typical emission pattern of an oscillating dipole is plotted in Fig. 4.2b. As one can see there is no light emitted along the direction of oscillation, whereas perpendicular to that the intensity has a maximum. Recording the scattered intensity, while slowly rotating the orientation of polarization of the guided light, would therefore allow to determine its polarization, which can be done by imaging the scattered light from the fiber.

For a sub-wavelength diameter nanofiber the polarization of a quasilinear polarized mode is given by Eq. (1.9)

$$\vec{E}_{\mathrm{lin}}^{(\omega f \varphi_0)} = \sqrt{2}A\left[\hat{r}e_r\cos(\varphi-\varphi_0) + i\hat{\varphi}e_\varphi\sin(\varphi-\varphi_0) + f\hat{z}e_z\cos(\varphi-\varphi_0)\right]\mathrm{e}^{if\beta z}, \quad (4.1)$$



(a) (b)

Fig. 4.2 a) Plot of the z-component of the electric field of a HE_{11}-mode polarized along the x-axis inside a nanofiber. The components of the field of guided light is sketched for a few positions, denoted with arrows and the corresponding excitation direction at the given position. For quasi-linear polarized light, the field points into the direction of the polarization axis φ_0 in the xy-plane, while the z-component varies according to its position. Note that the colour code denotes the phase of the z-component. b) Each scatterer on the nanofiber emits light in a dipole intensity distribution, where the emitted intensity depends on the polar angle θ, measured from the dipole oscillation axis. The shown case represents a scatterer on the fiber surface, oscillating along the x-axis as sketched in a). As one can see no light is emitted along the direction of polarization, and a camera (camera 1) looking this way will ideally detect no light. However, a perpendicular oriented camera will see the maximum of emitted light (camera 2).

where e_r, e_φ and e_z are the components of the mode function, $\hat{r}$, $\hat{\varphi}$ and $\hat{z}$ are the unit vectors of cylindrical coordinates, and φ is the orientation of the linear polarization with respect to φ_0.

As one can see, this mode has a non-negligible field oscillating in the direction along the fiber (z-axis), which will as well introduce dipole scattering. A close look at the field within the xy-plane (Fig. 4.2a) shows that the r and φ components of the guided mode add up to drive scatterers to oscillate along the polarization-axis φ_0 of the HE_{11}-mode. Superimposing the dipole emission pattern leads to an intensity distribution proportional to $\sin^2(\theta)$, where θ is the polar angle of the pattern (see Fig. 4.2b). Note that two perpendicular oriented cameras would see a phase, meaning a horizontal offset of the detected intensity as a function of polarization angle φ_0 of 90°.

The emission pattern of the z-component investigated on its own, depends on the spatial dependence of the phase of the z-component, which is colour-encoded in Fig. 4.2a. When considering a uniform distribution of scatterers in the fiber bulk and having linear polarized light along the x-axis ($\varphi_0 = 0$), observing the fiber via the vertical camera ($\theta = 0$) leads to full destructive interference of the emitted light, while observing along the horizontal axis ($\theta = \pi/2$) for the same polarization, allows the light, which is emitted from corresponding points on the fiber, to partially interfere constructively. Taking into consideration the additional scattering due to the z-component of the guided light, the term $\sin^2(\theta + \pi/2) = \cos^2(\theta)$ of the dipole emission in z-direction contributes to yield an intensity distribution proportional to $\sin^2(2\theta)$ with a constant offset. Therefore, for a proper determination of the polarization, the z-component needs to be filtered out before imaging the fiber, to be able to adjust the polarization reasonably. This can be done by placing suitable polarizing optics in the beam.

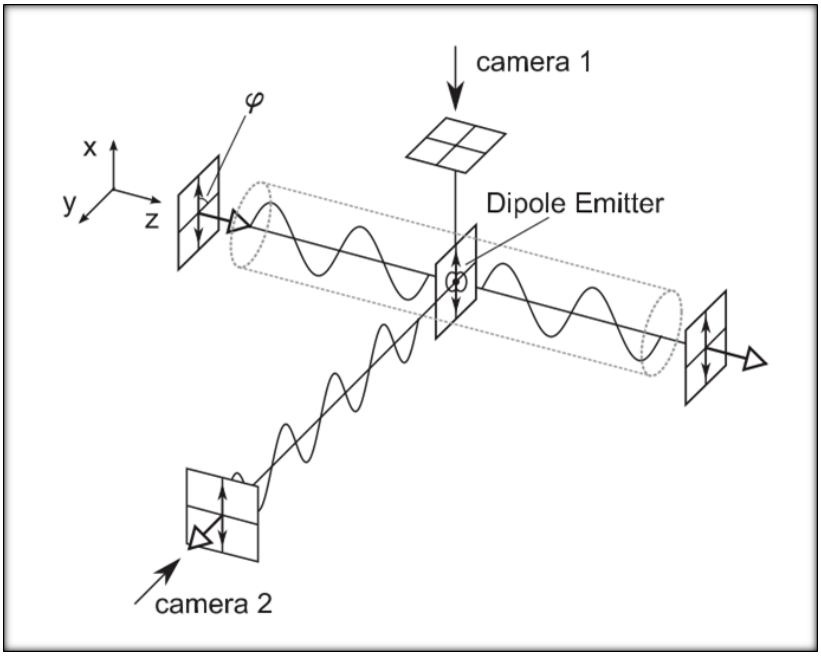


Fig. 4.3 A point-like emitter on the nanofiber is assumed to conserve the polarization of the fiber-guided light. Thus the dipole emission pattern will be aligned accordingly. Two cameras are imaging the fluorescence of the fiber in two perpendicular directions. Light polarized along the x-axis will be scattered and detected at camera 2 while camera 1 should not detect any light. Turning the polarization angle φ will change the intensities detected on the cameras, which allows to determine the polarization of light guided in the fiber. Taken from Vetsch et al. (2012).

To make sure that we have linear polarized light in the waist of the nanofiber, the fiber is imaged from two directions perpendicular to each other, as shown in Fig. 4.3.

In an ideal case, one camera should detect no light scattered from the camera while the other camera detects a maximum of intensity. Setting the polarization in the nanofiber is done with a $\lambda/2$ waveplate before coupling in the light into the fiber and the measurements map the detected intensity of scattered light to the waveplate angle φ. As a function of the waveplate angle, the detected intensity distribution should be proportional to $\sin^2(2(\varphi - \varphi_0))$, where φ_0 denotes the waveplate angle corresponding a linear polarization in the fiber along the x-axis. Note that the factor 2 occurs, since a $\lambda/2$ waveplate flips the polarization within a turn of 45°.

The parameter for optimisation in this method is the visibility of the fitted data, which is defined as

$$V = \frac{I_{\max} - I_{\min}}{I_{\max} + I_{\min}}, \tag{4.2}$$

where $I_{\max}$ and $I_{\min}$ are the maximum and minimum of the the fitted data, respectively. In an ideal case of quasi-linear polarized light, while filtering out the z-component, the visibility would be 100% and the angle corresponding to the axis of linear polarization φ_0 will not change across the fiber. Unfortunately due to the influence of small non-polarization maintaining scatterers the ideal visibility can not be reached. For the procedure of adjusting the polarization, the visibility will iteratively be maximized by compensating for parasitic birefringence in the nanofiber with a Berek-compensator in front of the fiber coupling. A Berek-compensator is a birefringent wavelength retarder that can be tilted in two directions and allows for arbitrary polarization transformations.

4.2 Design of the imaging setup

The advantage of the imaging setup designed in the context of this thesis is its compactness. To perform polarization imaging, the setup as introduced for absorption imaging remains almost unchanged. A few adaptations need to be made, i.e. placing polarization optics into the beam to guarantee suppression of contributions of the z-component of the electric field to the scattered light. To do so, in the horizontal imaging setup a nano-particle polarization filter is put exactly in front of the camera. In the vertical setup a $\lambda/2$ waveplate is put after the narrowing telescope, which acts as polarizer, when put in combination with the polarizing beam splitter, installed to separate the beam from the MOT-setup (see Fig. 3.9). Since the MOT-setup consists of a $\lambda/4$ waveplate for changing linear polarized light into circular polarized light for the purpose of having a MOT, an exchange of both waveplates has to be performed.

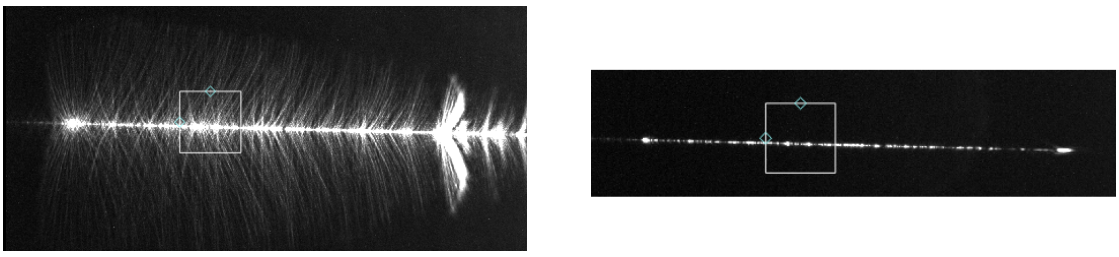
Changing between the two applications of the imaging setup can be done easily since both waveplates are mounted on flippable mounts.

Before starting the measurement one has to align the polarization optics carefully, since there is no direct possibility of aligning the $\lambda/2$ waveplate in a way that it will transmit the same polarization as the polarizer in the horizontal setup. One way of doing so is setting the nano-particle polarizer to only transmit vertical polarized light. One can rely on the vertical polarization, since the polarizer is pre-mounted and marked along the passing axis by the manufacturer and the extinction ratio of differently polarized light is very high (>100 000:1). After that, the polarization of guided light in the nanofiber is oriented in a way that the horizontal imaging system sees a maximum of intensity. According to the emission pattern of a dipole scatterer, the intensity in the vertical imaging should now be at its minimum (see Fig. 4.2a). This way the $\lambda/2$ waveplate can be adjusted to transmit, in combination with the PBS, a minimum of light. Thereby it is guaranteed that the same polarization is transmitted by both setups and the intensity recorded by the cameras can be analysed reliably.

The quality of the polarization adjustment in the nanofiber strongly depends on the maximal angle of the cone of light that can enter the first lens of the imaging setup. On the one side this angle should be as small as possible to only see a very small part of the intensity distribution of the dipole emission pattern, on the other hand an excellent nanofiber scatters only very little light, therefore a bigger cone of light entering the lens would be suitable. We decided on limiting ourselves on an opening-angle of about 5°. For the vertical imaging this is given naturally by the design of the setup. In the horizontal imaging a small iris is put into the setup to restrict the beam. Drawbacks in the total amount of light that reaches the cameras can be compensated with longer exposure times. Note that this way the data acquisition is prone to background light and suitable protection, such as lens tubes, has to be installed.

While setting up and testing the imaging setup for polarization measurements, it has been observed that the horizontal imagining system is prone to coma, an aberration similar to spherical aberration for objects further away from the optical axis, passing the lenses at an angle. Since the fiber is placed askew to the principal planes of the lenses, scattered light from the fiber is imaged by different zones of the lenses and therefore causing a coma. Even very careful alignment along 6 axes (3-spatial and 3 tilting axes) could not get completely rid of this aberration. The effect could be eliminated by placing an iris in the beam as entrance aperture. Note that an iris for coma compensation is usually put between the principal planes of an optical system, but due to spatial restrictions and the fact that anyway only one aperture can govern

the behaviour of the whole system, the iris for restricting the opening angle is also the iris for coma compensation (See Fig. 4.4).



(a) (b)

Fig. 4.4 a) Image of the fiber for a badly aligned lens system. Note that a fiber which is located askew to the lens system has different sections of the fiber imaged by corresponding zones of the lens. This results in a coma, seen as "fuzziness" of the image. b) Careful alignment and placing an iris in the beam allows to compensate for this aberration.

4.3 Data Acquisition and Analysis

The Data Acquisition is performed with a specially designed graphical user interface (GUI) to interact with the cameras and performing the analysis. Detailed description of the GUI can be found in Appendix A. The fiber will be imaged while one rotates the polarization coupled into the fiber stepwise by changing the waveplate angle φ and measures the scattered intensity. A full rotation allows for fitting the data to a $\sin^2(\varphi)$ and determination of the intensity minimum and maximum. To improve the measured visibility one settles on a minimum in scattered light and adjusts the Berek-compensator in a way to further minimize the intensity. Afterwards one repeats the procedure and iteratively maximizes the visibility.

The coupling of light into the fiber is done in a way, that the polarization alignment of the red-detuned, blue-detuned and resonant probe beam can be done individually. A result of a visibility measurement for resonant probe light guided through a test fiber located at ambient pressure is presented in Fig. 4.5, where the measurement for both cameras is shown. As one can see, the acquired data can be fitted very well to a $\sin^2(\varphi)$ and a visibility of 77.5% and 72% in the vertical and horizontal direction, respectively, could be achieved. The phase between the curves is of approximately 45° which corresponds to the perpendicular arrangement of the cameras. Note that the phase is 45° since we are using the angle of the $\lambda/2$ waveplate to map the polarization, which turns twice for a full rotation of the waveplate. After iteratively improving the

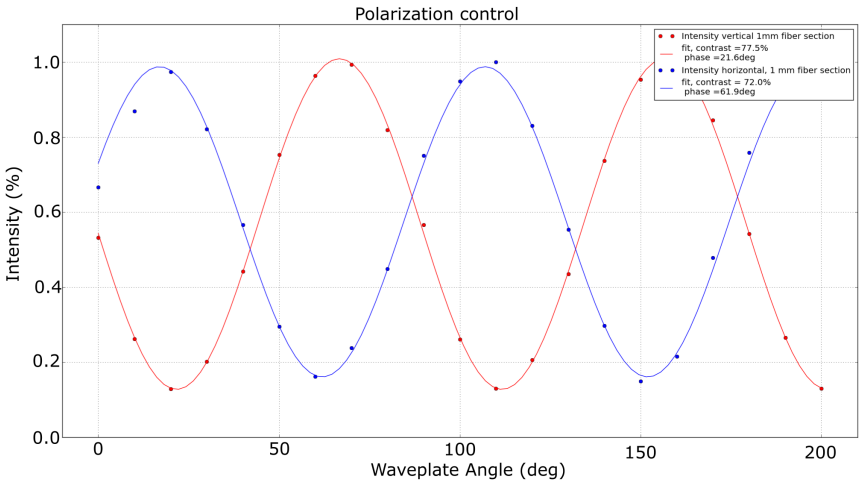


Fig. 4.5 Fitted data of the intensities detected in vertical (red) and horizontal direction (blue). The data was taken for a 1 mm long section of the nanofiber located in the middle of the waist.

visibility via adjustment of the Berek-compensator one could achieve visibilities up to 90%, as seen in Fig. 4.6. Note that one should always measure across short sections along the fiber since the visibility and angle φ_0 corresponding to the polarization along the x-axis change along the waist according to its birefringence. In Fig. 4.6 one can see, that the phase of the scattered light slightly changes for two sections of 0.4 mm on the far left and far right of the waist, which means that the polarization slightly rotates. Measuring a section containing light scattered from the whole waist leads to averaging over all amplitudes of light scattered into the direction of the camera.

Therefore the adjustments are carried out primarily for a small section in the middle of the nanofiber, and then, one uses the imaging setup to take pictures of the whole waist for every setting of the waveplate. The images are analysed for visibility and phase-relation of the polarization for several different spaced regions along the fiber (Fig. 4.7). Thereby one can determine whether the visibility and phase changes across the waist and determine a section where visibility is high and both phase and visibility remain constant for as long as possible. This information can be used to position the MOT accordingly and efficiently trap atoms in the desired region.

In the top plots of Fig. 4.7 one can see, that averaging over the whole fiber, considering sections of about 2.4 mm, seems to result in a rather constant visibility and phase. Looking at the bottom plots on the other hand, reveals that the local visibility and phase can change drastically. Possible reasons could be local variations in the

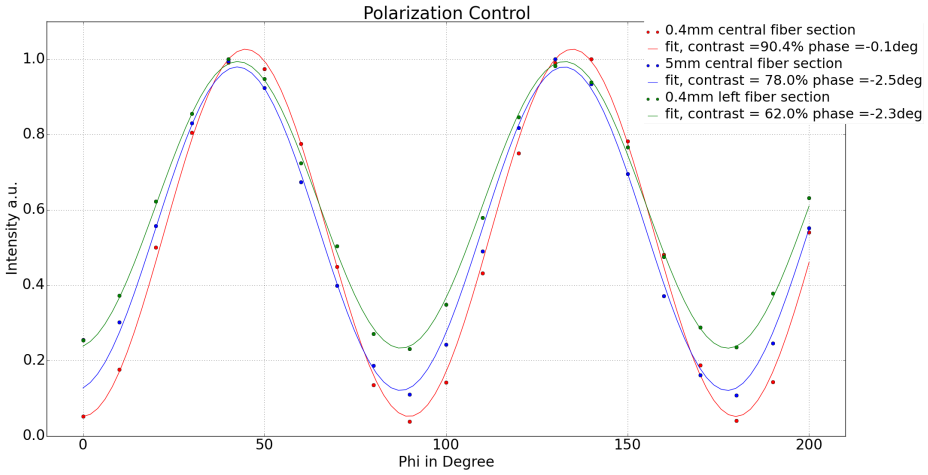


Fig. 4.6 Visibility measurements for three different sections across the fiber. On can see, that a very high visibility can be reached, but due to averaging of the amplitudes of scattered light over a bigger section of the fiber (blue), the visibility decreases.

density of inhomogeneities in the silica bulk or small dust particles on the fiber surface, which is possible since this fiber was tested in an exposed environment. Finally, for the last preliminary test, a fiber with a waist length of 10 mm was tested for the trapping light fields of 685 nm (blue-detuned) and 935 nm (red-detuned) wavelengths. The outcome of these measurements can be found in Fig. 4.8 and Fig. 4.9, respectively. Both show that the imaging setup and the iterative optimization process work sufficiently well for all required wavelengths. For the 635 nm laser the visibility could only be improved to be approximately 60%, where the visibility of the 852 nm and 935 nm laser was sufficiently high at the same time. For the purpose of testing the imaging setup and the optimization process only one Berek-compensator was used for birefringence compensation. In the implemented experiment, optimization can be done individually for each wavelength, since the fiber coupling setup is equipped with a $\lambda/2$ waveplate and a Berek-compensator in front of each coupler.

4.4 Summary and Outlook

In this chapter it has been shown how important the exact orientation of the polarization is for the successful implementation of a nanofiber-based dipole trap. Assuming small polarization maintaining scatterers on the fiber surface allows for indirect determination of the polarization orientation of the nanofiber guided light by measuring the intensity distribution of the scattered light, while turning the polarization in the fiber.

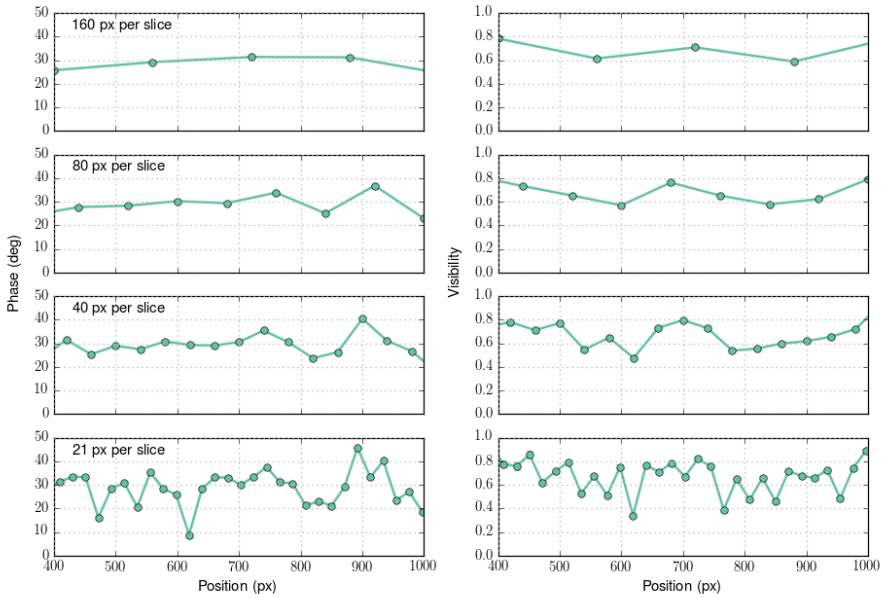


Fig. 4.7 Fiber analysis of a test-fiber performed by determining the visibility and orientation for differently sized sections of the fiber, guiding light of 852 nm wavelength. Using a coarse grain (top plot) leads to averaging over slightly changing values of the visibility which results in a rather constant plot. The second plot from the bottom analyses sections of an approximate size of 0.4 mm and is considered to reflect the local parameters the best. It is assumed that the dips seen in the bottom plot are dust particles, which corresponds in low visibilities due to assumed non-polarization maintaining scattering.

Experimentally it was possible to modify the implemented absorption imaging setup by adding polarization optics into the beam and successfully detect light scattered from the nanofiber via fluorescence imaging. The process of aligning the polarization optics correctly as well as the iterative process of optimizing the visibility of the scattered light to get well aligned linear polarization in the nanofiber has been discussed.

Preliminary measurements to align the polarization in test-fibers have shown that it is possible to achieve visibilities for small sections of the nanofiber up to 90%. Imaging the whole fiber showed that the averaged visibility across the whole fiber is about 70%, which is not yet satisfactory. Since the fiber was exposed to an open environment, dust settled on the fiber, leading to stronger scattering at a few points of the surface. Therefore smaller fluctuations of the intensity in sections in between could not be detected, since the strong scattering from dust particles already led to saturation of the camera. Additionally dust particles may not conserve the orientation of polarization and iterative improvement of the visibility could hardly be done to the full extend for

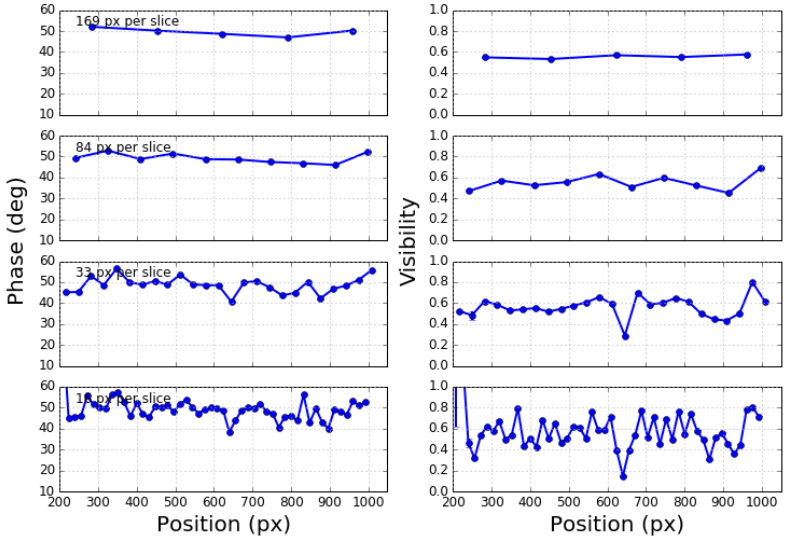


Fig. 4.8 Fiber analysis and determination of the visibility and orientation for differently sized sections of the fiber of 10 mm waist length guiding 635 nm wavelength light. As one can see, the visibility of approximately 60% is constant over the whole fiber, whereby the fluctuations seen for a very fine resolution of the measurement are a clear sign for an already very dusty fiber. The fiber was exposed to a lab-air environment for 2 days before taking this measurement.

a dusty fiber. Once a fiber is put in vacuum, dust particles and thus the restrictions in measurement as described above should not occur.

The fluorescence imaging and polarization measurements are necessary for the next step in setting up the experiment, since it allows for deciding whether the fiber put into the vacuum chamber fulfils the crucial requirements for further experimentation. This means having a fiber with a very high transmission and a long section of up to 10 mm with high values of a stable visibility and orientation of the polarization. If this can be verified, one can start trapping atoms and start to further characterise the nanofiber trap before performing the desired experiments.

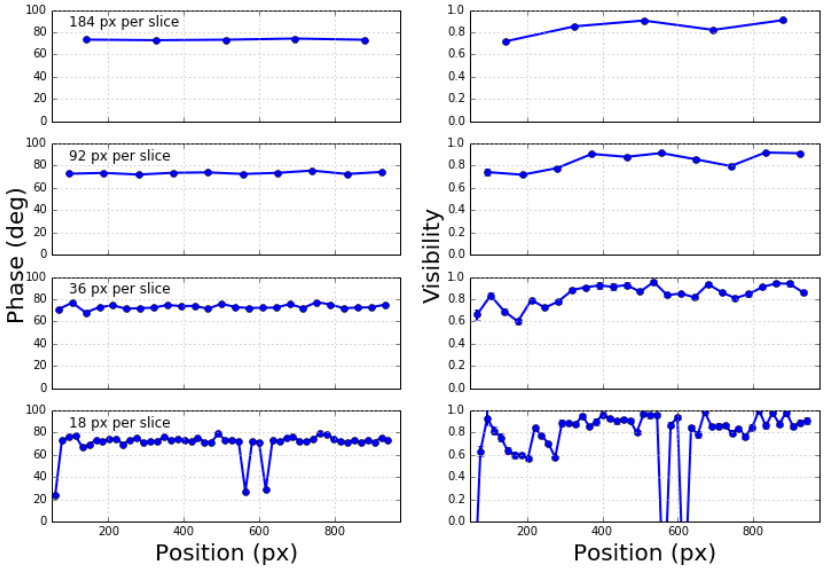


Fig. 4.9 Fiber analysis and determination of the visibility and orientation of 935 nm wavelength light for a 10 mm waist length fiber as described above.

Summary and Outlook

In this thesis, nanofibers were introduced as interesting devices for trapping Cesium atoms, for the purpose of investigating and using the light-matter interaction for quantum computational applications. I discussed a theoretical description of the guided electromagnetic waves in a sub-wavelength optical nanofiber and the possibility to trap atoms in potential minima of a combination of red- and blue-detuned light with respect to a resonant transition of a two level atom. State-independent trapping of Cesium atoms in close vicinity of a nanofiber can be done by using magical wavelengths, where an induced Stark-shift can be reduced to a minimum for D2-transitions. Furthermore, a trapping configuration was discussed, that will be used for the experiment, consisting of a red-detuned standing wave orthogonally linear polarized to a running blue-detuned wave. This way three dimensional trapping in (r,φ,z) directions in a distance of 200 nm from the nanofiber can be achieved. This standard trapping configuration is calculated to form potentials with an approximate depth of about 0.4 mK, which is why sufficient pre-cooling of the atoms is necessary. In this thesis, laser cooling and trapping mechanisms like magneto optical traps (MOT) and cooling via an optical molasses were theoretically discussed and the experimental setup to achieve cooling has been outlined. Once a cold atomic cloud is established, overlaying the optical molasses with the dipole potentials around the nanofiber allows for loading the nanofiber trap with Cesium atoms in close vicinity of the nanofiber surface. In this light-matter interface a high coupling strength between the fiber guided probe light and trapped atoms can be realized and further investigation, for instance for implementing a quantum memory, can be done.

Controlling and optimizing the whole cooling and trapping process requires the implementation of an appropriate imaging setup. The goal of this setup is the determination of the shape of the MOT-cloud and the polarization of the guided light-fields in the nanofiber. Designing this imaging setup required an investigation of physical and optical constraints. A theoretical discussion was given for the absorption of light in an optically dense atomic vapour, the behaviour of freely propagating cold atoms and their

velocity distribution for temperature determination. In addition, possible systematic errors in the imaging process were discussed. Based on this outcome, a two-lens system for imaging the shadow, cast by a probe beam while passing the atomic cloud, was designed and simulated. Analysis of the observed optical density of the atomic cloud allows for determination of the size, shape, position of the cloud and number of atoms in the cloud. Experimentally two imaging branches, one horizontally and one vertically oriented, were implemented and characterised to be in excellent accordance with the simulated parameters. Due to the compact design of the experiment, the vertical imaging arm is partially hosted by the MOT-laser distribution setup.

Furthermore, a theoretical description of the polarization of quasi-linear polarized light guided in the fiber was given. By assuming polarization maintaining scattering out of the fiber due to inhomogeneities in the bulk silica, determination of the a-priori unknown polarization in the nanofiber is possible. To do so, two cameras record the intensities of scattered light from the fiber, while the polarization in the nanofiber is turned by 2π. Necessary adaptations to the existing absorption imaging system have been implemented and the setup has been characterized to work successfully. Preliminary tests on a nanofiber in lab-air environment showed, that using the imaged fluorescence of the fiber allowed for compensation of parasitic birefringence in the nanofiber and optimisation of the linearities of the trapping field polarizations. The exact iterative process, where a combination of waveplates and Berek-compensators are used, has been described, and it is shown, that all three used wavelengths can be optimized sufficiently by this procedure.

Finally, for the acquisition of experimental results, a specialized programme to interface the cameras and analyse the recorded data was written and introduced in this thesis. The programme allows for a live view from the cameras, direct access to the camera settings, several real time measurement routines (e.g. rulers, intensity plots or region of interest control) and control over the time of flight measurement parameters.

Recently a nanofiber of 10 mm length and 200 nm radius was put into the vacuum chamber and sustained 50 mW coupled in laser power of 685 nm wavelength. In the next steps of setting up the experiment, the imaging setup is a very important application to decide, whether the fiber fulfils the crucial requirements for further experimentation. This means determination of a section of up to 10 mm with high values of visibility and a stable orientation of the polarization along the nanofiber. Additionally, it was possible to successfully implement a magneto optical trap of an approximate size of up to 10 mm $\times$ 2 mm size, and the first absorption images and time of flight measurements yielding lowest temperatures of 50 µK were taken. The next steps involve using these

technique for proper final alignment of the MOT-lasers, to create an atom cloud in the desired strongly elongated cigar shaped shape and to position it exactly above the nanofiber part of the fiber. After doing so, the cooling mechanism can be further characterised via time of flight measurements, to optimize the loading rate and number of trapped atoms. Finally, when the fiber trap and the cooling mechanism are carefully optimized, the nanofiber traps can be loaded and further experimentation can be performed.

References

Dalibard, J. and Cohen-Tannoudji, C. (1989). Laser cooling below the doppler limit by polarization gradients: simple theoretical models. *JOSA B*, 6(11):2023.

Estève, J. (2013). Cold atoms: Trapped by nanostructures. *Nature Nano*, 8(5):317.

Foot, C. J. (2004). *Atomic physics*. OUP Oxford.

Goban, A., Choi, K., Alton, D., Ding, D., Lacroûte, C., Pototschnig, M., Thiele, T., Stern, N., and Kimble, H. (2012). Demonstration of a state-insensitive, compensated nanofiber trap. *Phys. Rev. Lett.*, 109(3):033603.

Grimm, R. and Ovchinnikov, Y. (1999). Optical dipole traps for neutral atoms. *arXiv preprint physics/9902072*.

Le Kien, F., Balykin, V., and Hakuta, K. (2004a). Atom trap and waveguide using a two-color evanescent light field around a subwavelength-diameter optical fiber. *Phys. Rev. A*, 70(6):1.

Le Kien, F., Liang, J., Hakuta, K., and Balykin, V. (2004b). Field intensity distributions and polarization in a vacuum-clad subwavelength-diameter optical fiber. *Opt. Commun.*, 242(4):445–455.

Le Kien, F. and Rauschenbeutel, A. (2014). Anisotropy in scattering of light from an atom into the guided modes of a nanofiber. *Phys. Rev. A*, 90(2):023805.

Lett, P., Phillips, W., Rolston, S., Tanner, C., Watts, R., and Westbrook, C. (1989). Optical molasses. *JOSA B*, 6(11):2084.

Lewandowski, H., Harber, D., Whitaker, D., and Cornell, E. (2003). Simplified system for creating a bose–einstein condensate. *J Low Temp Phys*, 132(5-6):309.

Marangos, J. (1998). Electromagnetically induced transparency. *J. Mod. Opt.*, 45(3):471.

Raab, E., Prentiss, M., Cable, A., Chu, S., and Pritchard, D. (1987). Trapping of neutral sodium atoms with radiation pressure. *Phys. Rev. Lett.*, 59(23):2631.

Rauschenbeutel, A. (2009). Glasfasern Dünner als Licht. *Natur und Geist*.

Reitz, D. and Rauschenbeutel, A. (2012). Nanofiber-based double-helix dipole trap for cold neutral atoms. *Opt. Commun.*, 285(23):4705.

Reitz, D., Sayrin, C., Mitsch, R., Schneeweiss, P., and Rauschenbeutel, A. (2013). Coherence properties of nanofiber-trapped cesium atoms. *Phys. Rev. Lett.*, 110(24):1.

Sayrin, C., Clausen, C., Albrecht, B., Schneeweiss, P., and Rauschenbeutel, A. (2015). Storage of fiber-guided light in a nanofiber-trapped ensemble of cold atoms. *Optica*, 2(4):353.

Sesko, D. W. and Wieman, C. (1989). Observation of the cesium clock transition in laser-cooled atoms. *Opt. lett.*, 14(5):269.

Smith, D., Aigner, S., Hofferberth, S., Gring, M., Andersson, M., Wildermuth, S., Krüger, P., Schneider, S., Schumm, T., and Schmiedmayer, J. (2011). Absorption Imaging of Ultracold Atoms on Atom Chips. *Opt. Express*, 19(9):8471.

Steck, D. A. (2008). Cesium D line data. *Theo. Div.*

Vetsch, E., Dawkins, S. T., Mitsch, R., Reitz, D., Schneeweiss, P., and Rauschenbeutel, A. (2012). Nanofiber-Based Optical Trapping of Cold Neutral Atoms. *IEEE J SEL TOP QUANT*, 18(6).

Vetsch, E., Reitz, D., Sagué, G., Schmidt, R., Dawkins, S. T., and Rauschenbeutel, A. (2010). Optical interface created by laser-cooled atoms trapped in the evanescent field surrounding an optical nanofiber. *Phys. Rev. Lett.*, 104(20):1.

Warken, F. et al. (2007). *Ultradünne Glasfasern als Werkzeug zur Kopplung von Licht und Materie*. PhD thesis, Dissertation, Rheinische Friedrich-Wilhelms Universität, Bonn.

List of figures

1.1 Scheme of the nanofiber and its intensity distribution 2
1.2 SEM picture of the Nanofiber 2
1.3 Intensity distribution of the electric field of a linear polarized HE_{11} mode 5
1.4 Scheme of two-level atom and induced light shift 6
1.5 Experimental implementation of the nanofiber dipole trap 8
1.6 Typical trapping configuration 11

2.1 Two level atom in an optical molasses 15
2.2 Scheme of trapping via a MOT 16
2.3 Construction drawings of the vacuum chamber and breadboard construction 19
2.4 D2-transition of Cesium 20
2.5 MOT-beam distribution setup 21
2.6 MOT-beam alignment on breadboards 22
2.7 Beam shapes of the MOT-beams 23
2.8 Construction drawing of the magnetic coil setup 24

3.1 Scheme of the MOT-cloud expansion in TOF measurements 30
3.2 Scheme of a Kepler-telescope 31
3.3 Construction drawings of the glass cell 32
3.4 Scheme of the absorption setup 33
3.5 Ray tracing result of the horizontal imaging setup 35
3.6 Modulation transfer function (MTF) for the horizontal imaging setup . 36
3.7 Scheme of the horizontal imaging setup 37
3.8 Ray tracing result of the vertical imaging setup 40
3.9 Scheme of the vertical imagaing setup 41
3.10 Time of flight measurement after molasses cooling 44
3.11 Analysis of the TOF measurement 45

4.1 Scatterers on nanofiber 48
4.2 Dipole emission patern 49
4.3 Setup of the flourescence imaging setup 50
4.4 Allignment comparision for coma 53
4.5 Visibility measurement of one fiber by both cameras. 54
4.6 Visibility measurements for different sections across the fiber 55
4.7 Fiber analysis 852 nm 56
4.8 Fiber analysis 635 nm 57
4.9 Fiber analysis 935 nm 58

A.1 GUI Main Window 68
A.2 GUI Polarization Control for one camera 69
A.3 GUI Polarization Control for two cameras 71
A.4 GUI MOT Live Analysis 72
A.5 GUI TOF Analysis 73

Appendix A

Manual for Graphical User Interface

An integral part of the work, presented in this thesis, consisted in programming suitable tools to interface the cameras. Additionally a graphical user interface (GUI) was implemented, which allows for real time control of the cameras, data acquisition and real time displaying of images as well as plotting arbitrary user input vs. acquired data. The modules and the GUI is executed in Python[1]. The details of the code are described in Appendix B.

A.1 Main Window and types of programmes

The whole programme can be started by executing the file *Main_Window.py*, which can be found in the software folder of the experiments network drive. The main window represents an index of the whole programme-structure and executes the desired applications. (see Fig. A.1). The applications implemented are divided into programmes for investigation of the magneto optical trap and investigation of the polarization of the nanofiber. A detailed manual for each application can be found in the following sections. The programmes are:

1. **MOT Analysis**

   (a) Live Analysis

   Allows to view the MOT-fluorescence and to measure the size of the atomic cloud.

[1] recommended Python distribution: Anaconda for Phyton 2.7. For details see https://www.continuum.io/

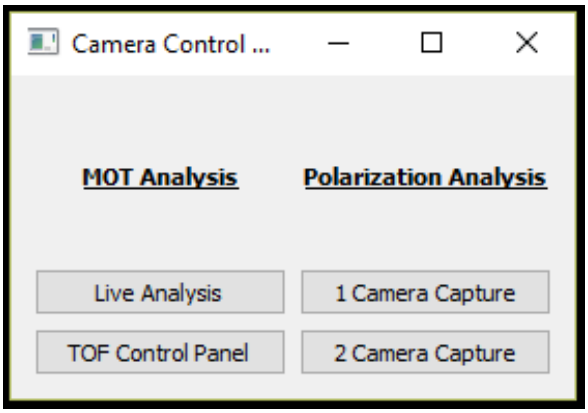


Fig. A.1 Main Window and starting point of the GUI. The buttons redirect to the according applications.

(b) TOF Control Panel

Use for starting the time of flight data acquisition and analysis.

2. **Polarization Analysis**

(a) 1 Camera Capture

Allows to measure and analyse the Polarization of the fiber with one camera.

(b) 2 Camera Capture

Allows to measure and analyse the Polarization of the fiber with both cameras simultaneously.

A.2 Polarization Analysis

The Polarization Analysis consist in two programmes, one for analysing the fiber with one camera at a time, the second one, to control both cameras simultaneously.

A.2.1 1 Camera Capture

The intention of this application is giving a live feed of the light scattered from the nanofiber, enabling plotting the measured intensity summed across a region of interest (ROI) versus the orientation of the waveplate, manipulating the polarization of the light, coupled into the fiber. Additionally a pre-analysis is performed and the data can be saved to the network drive. The camera that should be displayed can be selected in the drop down menu.

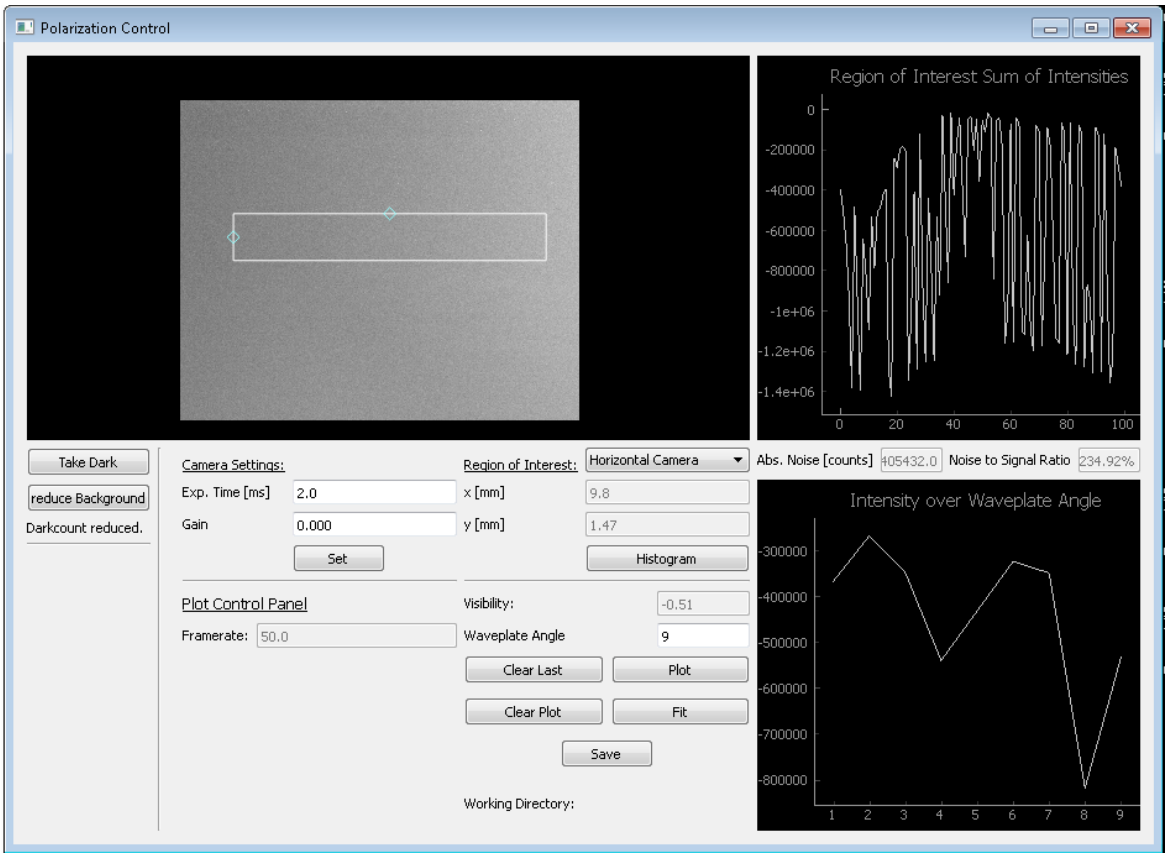


Fig. A.2 GUI Polarization Control for one camera

The GUI-window (see Fig. A.2) consists in three plotting widgets and a control panel. The main widget on the top left shows you a live feed of the acquired data and a selectable ROI, the top right widget displays the summed up intensity within the ROI and the bottom right widget plots user input versus the acquired intensity. The ROI can be moved and changed in size with the mouse.

The application is equipped with an automatic background reduction, which is subtracted from the ROI-data and already considered in the intensity plot. To take a dark image one has to press *Take Dark*. Note that whenever the size of the ROI is changed, the background needs to be subtracted by pushing *Reduce Dark*, otherwise the plotting widget freezes. The display will scale automatically, which might be inconvenient for some applications, but manually scaling is possible by using the mouse wheel.

The control panel consist in 3 main sections. The first section lets the user change the exposure time and gain of the camera by inserting the corresponding values and pressing *Set*. To find out whether the camera settings are chosen correctly for a good

dynamical range of intensity values, one presses *Histogram*. A separate window appears, plotting a histogram of the intensity distribution of the top left window.

The second section of the control panel gives the user information about the corresponding size of the ROI in real space. Additionally a small display shows the current frame rate, so one has an estimate if the programme is working correctly, since the frame rate will drop drastically for low exposure times, if the programme or camera crashes. If one detects a crash, usually re-plugging the USB connection works sufficiently.

The third section controls the user input for the plot widget to its right. The waveplate angle for polarization alignment is entered in the text-input-line and can be plotted by pushing *Plot*. The buttons *Clear Last* and *Clear Plot* clear the last entry and the whole plot, respectively. Clicking the *Fit* button will fit a $\sin^2(\varphi)$ to the plotted data and the corresponding visibility is displayed. To save the data, one has to enter an appropriate file description into the text edit and press *Save*. The plotted data is written to the experiments network drive and saved in a directory reading "Data\year\month\day\hour\Pol_\file description". For doing so, the time stamp of clicking *Save* is taken to create the directory.

While the programme is running, the data is already pre-analysed. The fluctuation and noise-to-signal ratio of the intensity is plotted underneath the top right plotting widget. Strong fluctuations indicate an unstabilized intensity of the laser or an unstable polarization, for instance due to thermal expansion of the glass-fiber, that is guiding the light from the laser table to the experiment table.

A.2.2 2 Camera Capture

This programme has exactly the same features as the *1 Camera Capture* programme and is extended to display and analyse data from both cameras at the same time. Note that the settings, ROI and background data have to be set individually.

As seen in Fig. A.3, the top two widgets display the horizontal camera, while the bottom two display data from the vertical imaging. The arbitrary plot window to the far right will plot data acquired from both cameras simultaneously, but save them individually (by pressing *Save*) for adequate further analysis.

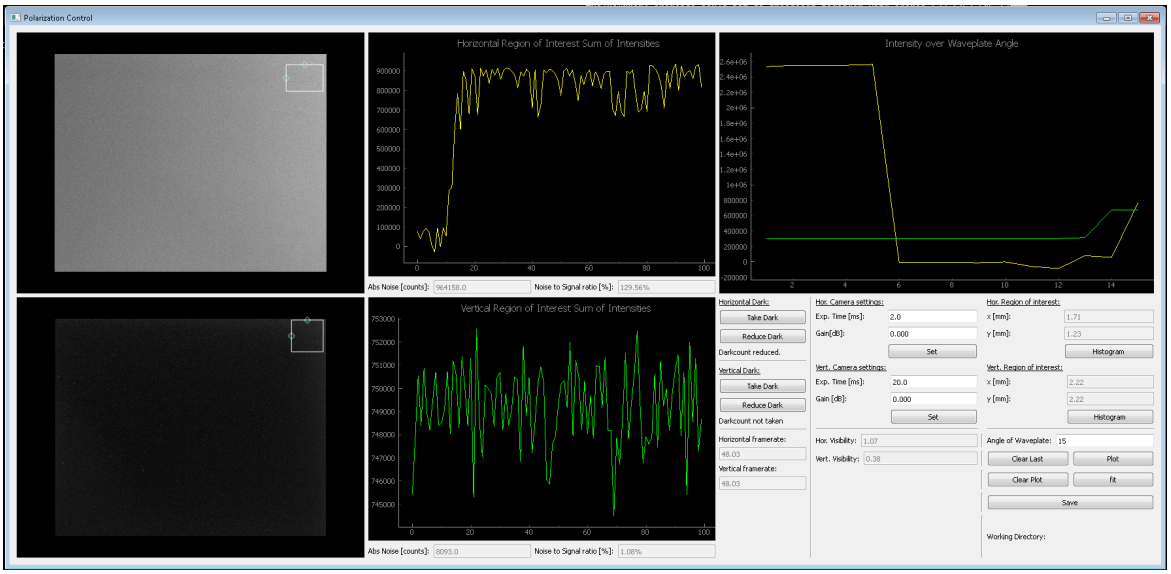


Fig. A.3 GUI Polarization Control for two cameras

A.3 MOT Analysis

A.3.1 MOT Live Analysis Programme

The MOT Analysis Programme (see Fig. A.4) is implemented for a live analysis of the MOT's fluorescence, for optimization and camera alignment purposes. In the top left window, the live data from one camera, selectable via the drop down menu on the right, is displayed. The red and yellow lines displayed on top of the live feed can be positioned by the user, and the intensities across them are plotted in the windows to the right (yellow line) and on the bottom (red line). By pressing *Fit*, a Gaussian is fitted to the last displayed data and remains plotted, while the live feed is continuing updating, to have a reference for optimization. The information withdrawn from the fits, is shown in the bottom of the programme. The control panel on the right side has the same features as in the applications introduced above.

A.3.2 MOT Time of Flight Data Acquisition Programme

The intended use for the time of flight programme is control and live surveillance of the time of flight measurements for temperature determination of the MOT.

As shown in Fig. A.5, the window on the left shows the live feed of the camera, which is selectable via the drop down menu. One has to make sure that the MOT-cloud is aligned appropriately, since the size and position will change during the course of the measurement. For alignment one can use the Live Analysis programme to look

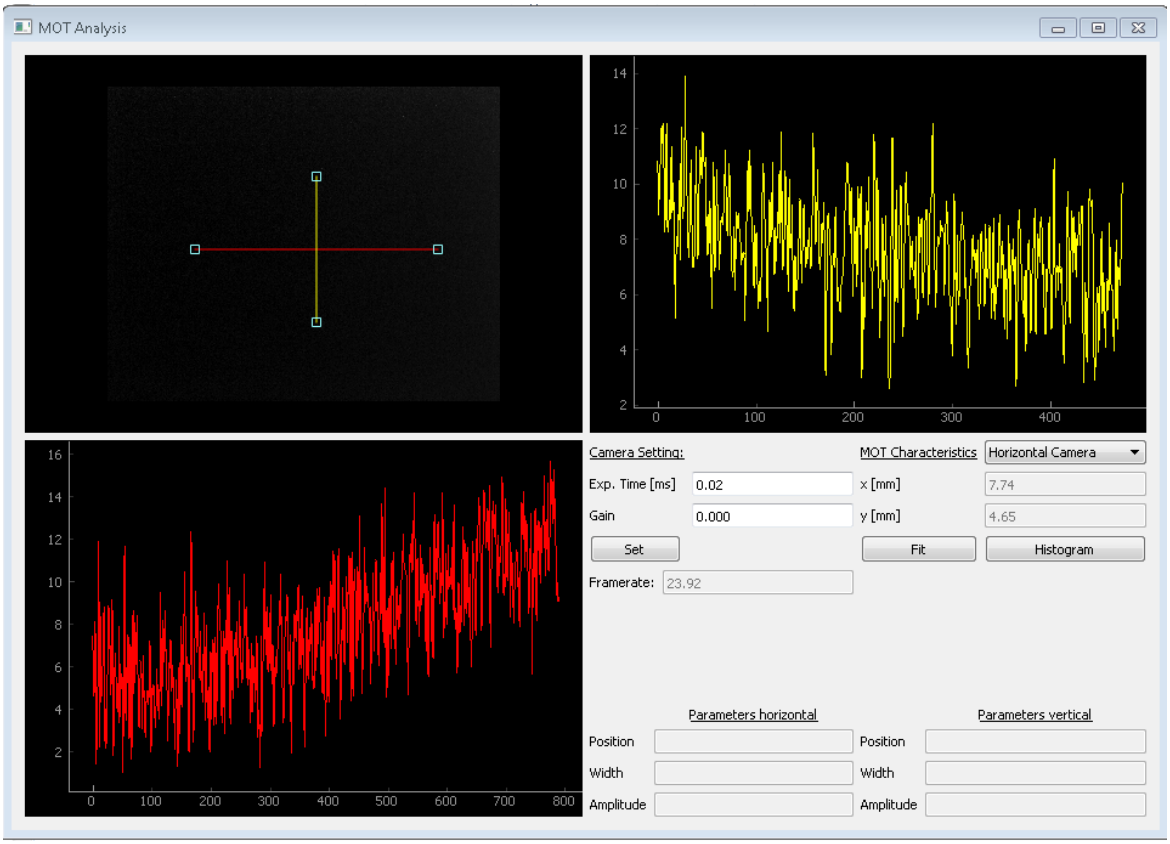


Fig. A.4 GUI MOT Live Analysis

at the fluorescence and change the displayed image section by tilting the last mirror before the camera.

The control panel on the right can be used to change the exposure time and gain of the cameras, by typing in the desired values and pressing *Set*.

Before one starts a measurement, one has to enter a suitable file description into the text edit and press *Save directory* to create a directory, where the acquired data is stored. The time stamp at pressing this button is use to create a directory "Data\year\month\day\hour\TOF_\file description". After doing so one has to enter the number of time steps one wants to acquire and press *Start TOF Measurement* to start the time of flight measurement. The camera will start a triggered acquisition mode, expecting three triggers per time step by the ADWin experimental control. Therefore, a suitable sequence has to be started in the corresponding software. Note that if the time between two triggers extends 2 seconds, the camera will give a timeout error and the programme might crash, which has to be considered in the experimental sequence.

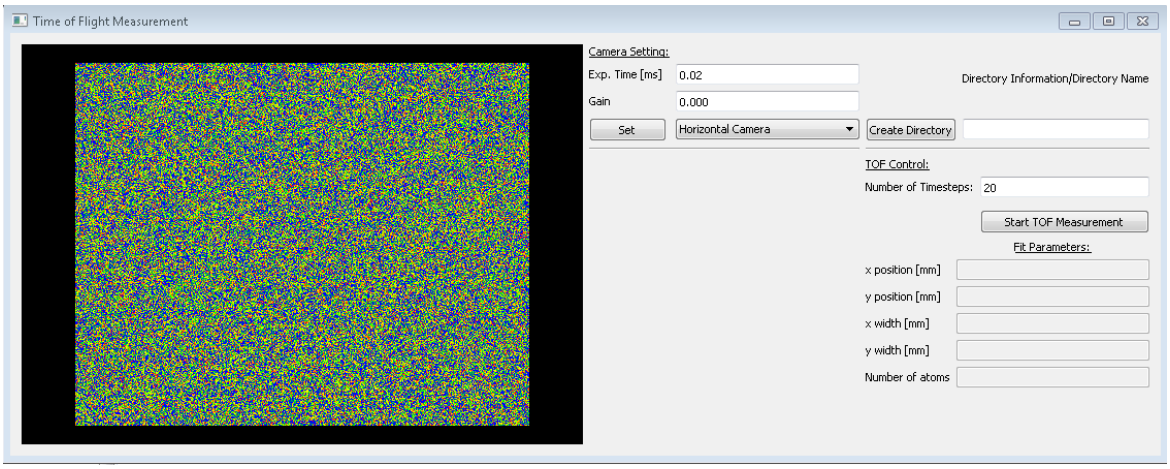


Fig. A.5 GUI TOF Analysis

The camera will then take a set of three pictures per step and analyse them regarding the centre, size of the MOT (densest place) and number of atoms. The results and reduced images will be saved in a stack of numpy arrays to the network drive in the corresponding directory. After the data acquisition, one can change to the Analysis software, to withdraw the saved data and determine the temperature via the expansion of the cloud. Note that the implemented default loading module will solely load the pre-analysed data, since loading all pictures takes some time. To load the images, one has to un-comment the corresponding line in the back-end modules.

Appendix B

Documentation on the code

The code written for absorption and fluorescence imaging consists in three main sections. The first section takes care of addressing the cameras allowing for adjustment of the settings and acquisition of data. The second section is for designing the graphical user interface (GUI) templates and the third section consist in the back-end for the GUI.

B.1 Data Acquisition and Analysis module

The most important part of the programmes, written in the context of this thesis, is the camera control and data acquisition module. The cameras are purchased from Matrix Vision and come with their own C, C++ and Net API called mvImpact Acquire[1]. The API already has a pre-installed GUI, but it does unfortunately not allow for direct access to the data. Since it was decided to have the whole experimental control setup in Python, a wrapper to translate the "pythonic" code into C++ and vice versa, to interface the camera is necessary. Fortunately such a code exists[2].

Accessing the camera is done by a programme called *modules.py*, which is structured in an object oriented way. The code allows for initializing the cameras, setting and querying settings, get a single and a triplet of pictures and adjusting trigger settings. The code is well documented in the code itself and only the rather unintuitive way of initialising the cameras is explained in detail here.

First the python wrapper *dmg* needs to be imported and assigned to a device with the regarding serial number, where F0800040 is the vertical and F0800038 is the horizontal camera. Since the cameras are built in a way to work in a stand alone configuration, without the need of a permanent computer connection, settings set

[1]Full documentation: https://www.matrix-vision.com/manuals/SDK_CPP/index.html
[2]Source code and documentation: https://github.com/geggo/MVacquire

for the camera will remain valid until changed. Therefore a manual reset has to be performed during initialization by setting the exposure time and gain to a default value and switching off the auto adjustment for both. Additionally the cameras have a maximum analog-digital converter (ADC) resolution of 10 bit. To avoid typecasting in later computation, the camera is forced to directly pass the 10 bit data. Finally, both the result and the request queue of the cameras are emptied, to ensure accurate measurements and correct assignment of the pictures. If a camera has to be re-initialized during the acquisition process or is switching to and from triggered mode, resetting the queues is done again to prevent possible Timeout errors.

The module additionally comes with an analysis object, which allows for loading the acquired data, calculating all desired MOT parameters such as central position, expansion and number of atoms, as well as time of flight analysis for temperature estimation.

This modules are the backbone of all back-end programmes that will link the functionality of the modules to the GUI.

B.2 Graphical User Interface

The GUI is programmed by using Qt[3] and Qt-Designer. Qt-Designer is a very straight forward tool for creating and designing a GUI-template, which then can be addressed by back-end programmes to accept user input and display all sort of output. A complete documentation of Qt and Qt-Designer can be found on the respective websites.

Unfortunately the real time plotting and displaying of images is a computational time consuming process. Note that Pythons standard plotting library Matplotlib cannot update data sufficiently fast and therefore is not suitable to use for real time displaying and plotting data acquired by the camera. Therefore pyqtgraph[4] is used, a specialised scientific graphical and GUI library, which can be connected to Qt and allows for fast imaging of data. To tell Qt to use the pyqtgraph imaging environment rather than its own, the widgets that should display pyqtgraph-content need to be manually changed to GraphicsView and PlotWidget (rather than QGraphicsView). To do so one has to promote the widgets by selecting the widget in the object-hierarchy on the top right in Qt-Designer and select *Promote to ...* and then manually enter GraphicsWindow, for displaying images, or PlotWidget, to allow for fast plotting. As source path it is sufficient to write pyqtgraph.

[3] http://www.qt.io/
[4] http://www.pyqtgraph.org/

The GUI templates are all stored in the camera software folder, located at the network drive of the experiment in the sub-folder *UI-Files*.

B.3 Back-end Modules

The back-end programmes merge the GUI template with the functionality of the data acquisition and analysis module. For each application introduced in Appendix A there exists a corresponding back-end programme. Each programme starts by linking the programme to the GUI-template by importing the *.ui* file. After that, the cameras, all buttons, ROIs, plot- and display widgets are initialised. Initialising means addressing the widget by its name, assigned in the *.ui* files via Qt-designer, and linking it to the functions executing the desired operations. As example given, a button is linked to a function setting the exposure time of the camera, whenever the button is clicked.

The most important part of the GUI is displaying data received from the cameras in real time, which is implemented for each programme and each camera respectively. This is done via two timers. The first timer continuously calls *readCamera*, which places an image request in the request queue and queries a result repeatedly until it gets one and restarts after that. By doing so it can be assumed that at all times the request and result queue consist in one picture maximally. This is done as fast as the camera allows, considering the exposure time. A second timer will trigger a function *updateCamera*, which updates the display and all computed values about 10 times per second. Note that this is purposely not done as fast as possible, since the data analysis and plotting takes a finite amount of time, during which the next picture would already be processed. That would lead to wrong assignments of computed data to the pictures and a time delay in displaying the data in the GUI. The updating function therefore will, whenever its called, take the last and in the way it is programmed, the only available image result. This result will be displayed and taken for further analysis. The pictures taken by *readCamera*, while the programme is processing the acquired data will be discarded. Note that this way, data acquisition and data analysis and display will work independently at all times, and the functions *readCamera* and *updateCamera* will never be idle. This prevents the programme from having delays in displaying the acquired data, wrongly assigning images to acquired data and crashing of the programme due to timeout errors.

Besides that, every programme consists in a series of functions that compute data according to the purpose of their application. The most important functions are summarized below:

1. **readCamera** Reads the buffer of an image result, received from the camera, and casts it into a numpy array. After that, the buffer is deleted and a new request placed on the camera. Note the timeout must not be set to 2 seconds, since the camera will not recognize a timeout of exactly 2 seconds and will return an error.

2. **updateCamera** Depending on the application this function will display the image in the ViewBox of the GUI. Additionally, it will sum up the intensity across the ROI and plot the value in one of the plot widgets. Besides that, in some programmes this function will calculate fluctuations and signal-to-noise ratios of the plotted data, display the size of the ROI and warn in case of saturation of the camera.

3. **TOF_acquisition** This function stops immediately all timers and the continuous data acquisition. The result and request queues are reset to prevent timeout errors and guarantee correct trigger to picture assignment. The number of sequences, the user wishes to take, is saved for a while loop, and the timers for triggerd acquisition are connected to the function *readCamera_triggered* and started to run as fast as possible.

4. **readCamera_triggered** This function calls *module.py* functions to acquire three triggered images, with MOT-cloud, without MOT-cloud and background, respectively, and passes the data for pre-analysis. The result of this images is stored in a 3D-numpy array (3:1280:1024), where each layer corresponds to an image of 1280 $\times$ 1024 pixels. The result is then passed to be post-processed (image subtraction and optical density calculation) and analysed for size, centre and number of atoms. The post-processed picture and all received values are stored and displayed in the GUI, so one has an insight of what is going on during the measurement. After the acquisition finished the GUI continues to continuously acquire and display images.